Additive Manufacturing 55 (2022) 102785

Contents lists available at ScienceDirect

Additive Manufacturing

journal homepage: www.elsevier.com/locate/addma

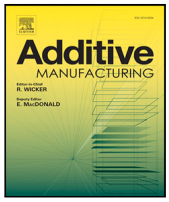

Research paper

Liquid–solid co-printing of multi-material 3D fluidic devices via material jetting

Brandon Hayes, Travis Hainsworth, Robert MacCurdy *

University of Colorado Boulder, Department of Mechanical Engineering, Boulder, 80309, CO, USA

ARTICLE INFO

Keywords:
Additive manufacturing
Mesofluidics
Modeling and simulation
Multi-material
Material jetting

ABSTRACT

Multi-material material jetting additive manufacturing processes deposit micro-scale droplets of different model and support materials to build three-dimensional (3D) parts layer by layer. Recent efforts have demonstrated that liquids can act as support materials, which can be easily purged from micro/milli-channels, and as working fluids, which permanently remain in a structure, yet the lack of a detailed understanding of the print process and mechanism has limited widespread applications of liquid printing. In this study, an "all in one go" multi-material print process, herein termed liquid–solid co-printing in which non photo-curable and photo-curable liquid droplets are simultaneous deposited, is extensively characterized. The mechanism of liquid–solid co-printing is explained via experimental high speed imaging and computational fluid dynamic (CFD) studies. This work shows that a liquid's surface tension can support jetted photopolymer micro-droplets which photo-polymerize on the liquid surface to form a solid layer of material. Design rules for liquid–solid co-printing of micro/milli-fluidic devices are presented as well as case studies of planar, 3D, and multi-material micro/mesofluidic structures such as mixers, droplet generators, highly branching structures, and an integrated one-way flap valve. We envision the liquid–solid co-printing process as a key new capability in additive manufacturing to enable simple and rapid fabrication of 3D, integrated print-in-place multi-material fluidic circuits and hydraulic structures with applications including micro/mesofluidic circuits, electrochemical transistors, lab-on-a-chip devices, and robotics.

1. Introduction

Additive manufacturing was introduced commercially in 1987, and has recently begun the transition from a rapid prototyping tool used to produce individual components into a viable approach for the direct fabrication of entire integrated systems [1–4]. This convergence is enabled by multi-material deposition in which materials with heterogeneous properties are simultaneously, rapidly, and precisely deposited, yielding functional print-in-place assemblies that require little to no additional fabrication effort. Material jetting three-dimensional (3D) printing will play an important role in this transition because it combines high throughput, seamless and rapid deposition of multiple materials (including mixing), a large build volume, and fine resolution. In this work, we present a key contribution to this ecosystem: liquid–solid co-printing which entails co-deposition of solidifying and non-solidifying materials in a multi-material material jetting process. Solidifying materials, such as phase changing inks, harden and exhibit a dramatic increase in shear modulus soon after deposition whereas non-solidifying materials remain a liquid after deposition. By combining these two material classes in a multi-material material jetting 3D-printing context, we enable liquid support that is trivial to remove, and allow liquid-phase materials to be embedded within a printed *multi-material* object. By depositing liquids as *working fluids*, this approach enables direct deposition of chemical reactants, and solves a longstanding challenge in material jetting additive manufacturing: how to clear long tortuous internal channels after 3D-printing. We anticipate that liquid–solid co-printing via multi-material material jetting will enable unique 3D-printed geometries in applications spanning fluidic logic circuits, electrochemical sensors and amplifiers, microfluidics, lab-on-a-chip devices, and robotics.

Numerous additive manufacturing approaches have been used to fabricate parts containing internal cavities or fluid channels, with applications spanning robotics to microfluidic reactors. These methods include fused deposition modeling (FDM) [5,6], stereolithography (SLA) [7–9], digital light processor stereolithography (DLP-SLA) [10,11], and two-photon direct laser writing (DLW) [12–14]. Material extrusion methods employing one or more individual nozzles are often called direct ink write (DIW) and have been used to create support

* Corresponding author.
E-mail address: maccurdy@colorado.edu (R. MacCurdy).

https://doi.org/10.1016/j.addma.2022.102785
Received 27 January 2022; Received in revised form 14 March 2022; Accepted 21 March 2022
Available online 14 April 2022

material that is evacuated in post-processing to form the void spaces of a soft fluid-pressure actuated robot [15]. A similar fabrication approach using cell-laden fugitive inks extruded into a sacrificial support bath yielded vascularized heterogeneous tissue constructs [16]. While material extrusion methods, including FDM and DIW, have broad material applicability and allow multiple materials in the same printed object, they fundamentally compromise fabrication speed and resolution, since each material must pass through a dedicated nozzle that is scanned over the build region, and only one nozzle is active at a time. The material extrusion approach was recently scaled in a multi-material context by linking many parallel nozzles to a small number of pressure-controlled fluid channels [17]. This approach increased print speed, but only when the printer produced regular repeating patterns that matched its nozzle array. Vat photopolymerization approaches like SLA, DLP-SLA, and DLW employ a volume of photo-resin and expose it by rastering or projecting an image. While these techniques can have resolutions as fine as 100 nm [18], or build volumes exceeding the size of a basketball [19], no current system offers very fine resolution (< 150 μm) and a large build volume simultaneously. Additionally, though exposure control can offer spatially-varying mechanical properties [20,21], these methods are effectively single-material. Research systems that extend vat photopolymerization to multiple materials [22] currently suffer from slow print speeds because they must switch between materials at every new layer, and operation with heterogeneous print material properties remains a challenge. Similarly, DLW systems, while enabling heterogeneous print materials, suffer from slow print speeds as they must raster a laser to selectively polymerize photo-resin, making such approaches ill-suited for multi-scale prints where both fine resolution features and a large print volume are required [23,24]. In summary, FDM, DIW, SLA, and DLW are used widely and offer diverse material selections, but impose significant design constraints. These constraints, depending on the specific 3D-print modality, include various combinations of: low resolution, slow print speeds, small build sizes, and either single-material operation or slow transitions between different print materials. As a consequence, designers of fluidic circuits or systems that integrate heterogeneous materials with applications as diverse as soft robotics [25] and wearable devices [26,27] must currently employ labor-intensive methods that often combine lithography, macroscopic molding, and additive manufacturing of individual components interspersed with manual assembly steps [28–30].

Material jetting 3D-printing (also known as PolyJet [31] or MultiJet Modeling [32]) deposits micro-scale droplets of material using inkjet technology. As such, it offers rapid transitions when depositing dissimilar materials during a print and high throughput relative to other additive manufacturing approaches, while providing a large build volume (> 30 liters is common) with feature sizes below 150 μm [33]. Accordingly, it has been used to fabricate soft robotics with embedded fluid circuits [34–36], and devices with microfluidic channels [33,37–39], albeit with significant manual post-processing. Material jetting offers a unique capability in the Additive Manufacturing context: rapid and precise deposition of picoliter-scale droplets of dissimilar inks [40], adjacent to each other and at nearly the same time, enables materials with widely varying electromechanical and chemical properties to form composite materials with visual and mechanical gradients [41], active parts including semiconductors and electrical circuits [42–44], and functional "print-in-place" objects requiring no additional assembly [36,45,46]. As such, it presents a potential path toward convergent, integrated manufacturing of entire print-in-place functional systems.

In contrast to additive manufacturing approaches like SLA and FDM, material jetting printing requires a fully-filled layer of material to support each successive layer; that is, it needs something to print "on top of" because it prints objects from bottom to top. When the material that supports subsequent layers occupies a region that will eventually be a void (or empty) space, the material is referred to as a sacrificial "support" material. There are two primary techniques to support the ink that will form the top (herein referred to as the "capping layer", Fig. 1) of a void space in a material jetting process: (1) the use of phase-changing sacrificial fugitive inks [37,47–51] and (2) the use of non phase-changing inks [52,53]. Phase-changing fugitive inks can be photo-curable support material as is common in the Stratasys PolyJet printers or thermal phase-changing materials such as wax, common in 3D Systems multiJet modeling (MJM) printers. For the former, the shear modulus of solidified photo-curable support material makes it impossible to remove from micro/mesofluidic channels that are long and narrow using fluid pressure alone [39]; this makes photocuring support material impractical to use with micro/mesofluidic systems [54]. In contrast, thermal phase-changing support materials enable fabrication of micro/mesofluidic channels since they can be melted and flushed away [35,37]. However, the post-processing required to remove thermal phase-changing materials is often extensive, and involves a closed-loop pressure-driven continuous flush with hot (80 °C) mineral oil to dissolve and remove wax from channels [35]. Accordingly, as the micro/mesofluidic channels become more tortuous, phase-changing materials become increasingly difficult to fully remove, as wax purge ports must be integrated and then later sealed at each potential branch or eddy point in the fluidic circuit [35]. In a large-scale 3D meso/microfluidic system, such as a soft robot with fluidic logic, or an integrated microfluidic system, sealing hundreds of wax removal ports is arduous if not impossible, and imposes a significant design constraint because the purge ports must be routed to an exterior surface for connection to the purging-pump system. Also, the use of high temperatures to melt wax places additional constraints on resin selection to prevent thermal warping, and makes the print process incompatible with printing biologically relevant liquids or reagents that might be temperature sensitive.

We first introduced liquid–solid co-printing in 2015 for the fabrication of hydraulic structures and robots using liquid as a support material as well as a working material in the PolyJet print process [36]. In liquid–solid co-printing, a PolyJet printer simultaneously deposits photo-curable droplets (resulting in a solid region) and non photo-curable droplets (resulting in a liquid region) to create hydraulic structures (see Fig. 1). This fully automated process enables fabrication of complex 3D multi-material hydraulic structures. We fabricated fully functional 3D printed bellows with fluidic channels on the order of mm–cm's. Later, Castiaux et al. demonstrated a pause–print–pause PolyJet print process capable of directly fabricating microfluidic structures by printing open channels, pausing the print, manually filling void space with liquid, and resuming the print [33,55]. The use of liquid as a support material instead of conventional photo-curable soluble support enabled Castiaux et al. to fabricate PolyJet-printed serpentine *planar* microfluidic channels which had previously been nearly impossible to fully purge of support material [56]. We observe that pause–print–pause workflows are compatible with 2.5-dimensional (layered) geometries, but not 3D. Due to the required intermittent pausing in the pause–print–pause print process, it would be impractical to fabricate fully 3D micro/milli-channels (such as 3D spirals) of arbitrary cross-section or integrated multi-material valves and fluidic interconnects using this workflow. As such, there is a need to extend the fully automatic approach of liquid–solid co-printing into micro/mesofluidics with fluidic channel cross-sections on the order of 100-1000 μm. Additionally, our past work and Castiaux et al. focus on the application of using liquid as a support material to build specific channels. No work to date has studied the physical mechanisms that underpin using liquid as a support material nor characterized the liquid–solid co-printing print process to enable the general use of this print technique.

In summary, despite the many advantages of material jetting 3D printing, the requirement for fully-filled solid layers (no voids), and the reliance on phase-changing support materials makes current multi-material material jetting printing processes ill-suited for fabricating tortuous internal channels, or other regions that will be empty space or filled with working fluids within an otherwise solid object. The present work addresses this challenge by extensively characterizing a

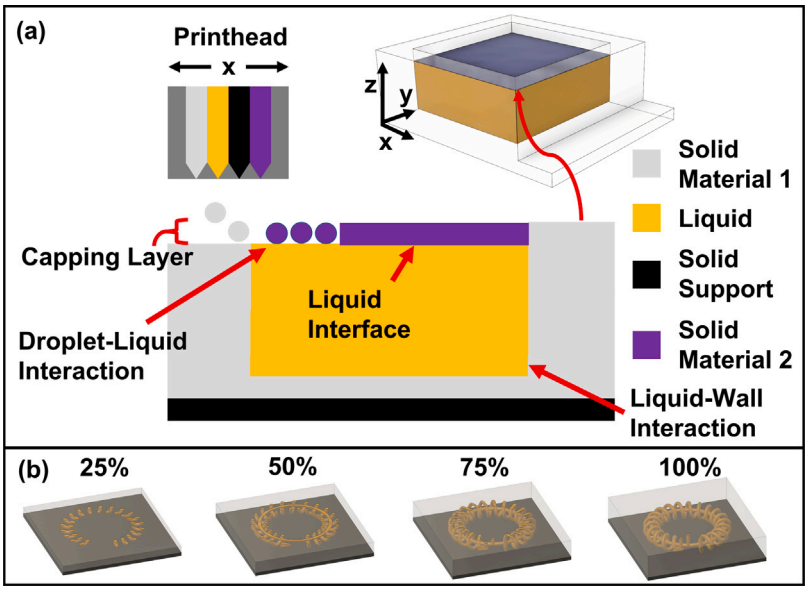

Fig. 1. Liquid–Solid Co-Printing Mechanism Schematic — depicts a schematic representation of the liquid–solid co-printing print process as a deposition head scans across the build region. (a) Non photo-curable material is deposited to build a liquid region defined by an arbitrary STL or voxel design. Two primary interactions are highlighted: (1) liquid–wall interaction and (2) droplet–liquid interaction. As the liquid is deposited, it is contained by the surrounding photo-curable material giving rise to liquid–wall interactions. Once the last liquid layer is deposited, the capping print layer (defined as the first photo-curable material layer on top of the liquid support region) deposits photo-curable droplets on the liquid interface giving rise to droplet–liquid interactions. Not shown in the schematic are UV lights to cure the resins and the "roller" which smooths droplets for each print layer. Here, solid material 1 and solid material 2 are VeroClear and VeroCyan respectively. (b) Time evolution of the print process is shown at 25%, 50%, 75%, and 100% completion of the object displayed in Fig. 9b.

multi-material material jetting printing approach using non-solidifying (liquid) materials as inks that can be: (a) employed as support materials that can be easily flushed from complex, 3D multi-material micro/mesofluidic channels and, (b) be permanently embedded as working fluids within a 3D-printed object.

In this study we present the mechanisms, capabilities, and constraints behind liquid–solid co-printing, and extensively characterize the process. We demonstrate the ability of this technique to enable planar, 3D, and multi-material micro/mesofluidics since liquid can be easily purged from micro/mesofluidic channels by applying a modest pressure differential to the channel [52,53]. Additionally, the low viscosity of the liquid support allows tortuous (highly-branching, see Fig. 9c,d) channels to be easily purged with a single connection. Although many of the examples shown in this study use liquid which is later purged as a sacrificial build material for micro/mesofluidic devices, liquid can be thought of more generally as an material jetting *working material*, like any other material in the printer's palette. In this sense, liquid is not purged from a device and instead is critical to device functionality such as in printed hydraulic structures or the deposition of encapsulated reagents in a microfluidic reactor [36,57].

Liquid–solid co-printing holds the potential to directly fabricate 3D multi-material micro/mesofluidic circuits in which complex fluidic channels, interconnects, valves, and pumps can be printed in situ without extensive post-processing, driving advances in applications of fluidic logic. This work provides the framework to:

1. Understand micro-scale interactions between photo-resins and a liquid interface
2. Provide design guidelines including minimum channel feature sizes for PolyJet liquid–solid co-printing and a method to determine these parameters from similar printer systems
3. Design and fabricate multi-material micro/mesofluidic devices including flexible valves in accordance with liquid–solid co-printing design rules.

While the experimental setup for this paper employed a Stratasys J750 material jetting 3D printer, the methods and analysis described here are applicable to other commercially available printers which use similar materials and deposition methods. We envision this liquid–solid co-printing print process as a general approach to enable simple and rapid fabrication of 3D, multi-material micro/mesofluidic circuits, with diverse applications spanning soft robotics, biomedicine, and visual arts.

2. Liquid–solid co-printing theory and mechanism

Figure 1 and movie S5 describe the liquid–solid co-printing process. Following the normal PolyJet method, the process starts by depositing an initial layer of rigid material to promote adhesion to the build platform, followed by several layers of solid support to provide structural stability and a uniform base for the printed part. Photo-resin droplets are then deposited in accordance with the design geometry. Unlike the normal PolyJet print process, liquid–solid co-printing deposits non photo-curable material (in this work we used Stratasys model cleaning fluid, herein referred to as "liquid" or "non-solidifying fluid") to build a liquid region defined by an arbitrary STL or voxel-definition design. Note that "voxel" refers to a volumetric-pixel, the minimum addressable volume in a 3D printer, and designs can be defined by specifying the type of material meant to be in all available voxels. The amount of liquid deposited can be controlled by varying the piezoelectric actuation voltage (further discussed in Section 3.1), allowing liquid material to be under- or over-jetted (defined as when the liquid amount deposited in each droplet is below or above the target voxel volume, respectively). As the liquid is deposited, it is contained by the surrounding photo-curable material (which is deposited at the same time) giving rise to *liquid–wall interactions*. Once the capping layer (defined as the first photo-curable material layer on top of the liquid region) is reached, photo-curable droplets are deposited on the liquid interface giving rise to *droplet–liquid interactions* which enables liquid to behave as a material jetting support material. Not shown are the UV lights to polymerize the resins and the integrated "roller" which ensures planar layers and removes excess material with each print layer scan. The roller affects droplet–liquid interaction as well as liquid–wall interaction and plays a significant role in the liquid–solid co-printing process which is characterized in Section 3.3.

2.1. Droplet–liquid interaction physics

Liquid–solid co-printing can be simplified to a 2-phase flow problem during fluid deposition and a 3-phase flow problem during droplet–liquid interaction (prior to photopolymerization, and when fluid–structure interactions between the roller and jetted material are neglected). Consider the construction of the design shown in Fig. 1, which is fabricated from the bottom-up, layer by layer. Before the capping layer, liquid droplets impact a liquid pool of the same material. This is a 2-phase flow problem. Upon reaching the capping layer, photo-resin droplets impact a dissimilar liquid surface. This is a 3-phase flow problem. While simplified, a reduced order 2-phase and 3-phase flow model of liquid–solid co-printing can provide insights into the fluid dynamics of the print process. Computational modeling of the fluid–structure interaction between the roller and jetted material, and photopolymerization effects is beyond the scope of this work and will be the subject of future modeling studies.

In the simplified 2-phase model, both FLOW-3D and OpenFOAM are used to simulate droplet impact. FLOW-3D cannot model 3-phase flows and thus, for 3-phase flow, the 3-phase incompressible, laminar, sharp interface fluid solver *multiphaseInterFoam* in OpenFOAM v2012 is used to study droplet–liquid interactions. The three phases present in liquid–solid co-printing are: (1) air, (2) non-solidifying fluid, (3) photo-curable resin. Interfaces are captured using the volume of fluid (VOF) phase field method with interface compression [58] for each phase denoted by α_i. Specifically, $\alpha_i \in [0,1]$ and $\sum_{i=1}^{i=3} \alpha_i = 1$ for each cell element. A mixture density (ρ) and viscosity (μ) is used by weighting the phases within each cell element where

$$\rho = \sum_i \alpha_i \rho_i \tag{1}$$

and

$$\mu = \sum_i \alpha_i \mu_i. \tag{2}$$

The incompressible Navier–Stokes equations are then solved as follows accounting for interfacial tension forces [59]:

$$\nabla \cdot \mathbf{u} = 0 \tag{3}$$

$$\rho\left(\frac{\partial \mathbf{u}}{\partial t} + \mathbf{u} \cdot \nabla \mathbf{u}\right) = -\nabla p + \nabla \cdot \tau + \mathbf{F}_{st} + \mathbf{F}_g \tag{4}$$

where $\mathbf{u}$ is the velocity field, p is the pressure, τ is the stress tensor, $\mathbf{F}_{st}$ is the surface tension force, and $\mathbf{F}_g$ is the gravitational body force. The stress tensor for a Newtonian fluid is defined as

$$\tau = \mu\left(\nabla \mathbf{u} + (\nabla \mathbf{u})^T\right). \tag{5}$$

The surface tension force is given by

$$\mathbf{F}_{st} = \gamma\left(\nabla \cdot \left(\frac{\nabla \alpha}{|\nabla \alpha|}\right)\right)\nabla \alpha \tag{6}$$

where γ is the surface tension. The gravitational force is given by

$$\mathbf{F}_b = \rho g \tag{7}$$

where g is the gravitational acceleration. These equations are solved using the multi-dimensional limiter for explicit solution (MULES) algorithm. An adjustable time step formulation based on the Courant–Friedrichs–Lewy (CFL) criterion is utilized in the temporal numerical scheme with a maximum CFL number set to 0.50 to ensure stability. Phases are tracked by solving the phase fraction advected through each fluid with interface compression:

$$\frac{\partial \alpha_i}{\partial t} + \nabla \cdot (\alpha_i \mathbf{u}) + \nabla \cdot \left(U_r \alpha_i (1 - \alpha_i)\right) = 0. \tag{8}$$

U_r is the numerical applied velocity field used to compress the interface given by

$$U_r = C_\alpha \frac{\nabla \alpha_i}{|\nabla \alpha_i|} \tag{9}$$

where C_α is a binary term $\{0,1\}$ to toggle interface compression [60]. Realistically, as a photo-resin polymerizes, its liquid density and viscosity increase ultimately behaving as a solid region upon complete photopolymerization. It is important to note that the Stratasys liquid resins used in this study are less dense than the non-solidifying liquid prior to polymerization but, after polymerization, become more dense than the non-solidifying liquid (see table S2).

2.2. Mechanism

Here, the mechanism behind liquid–solid co-printing is presented. In the Stratasys J750 printer, piezoelectric inkjet droplets are of the order of D = 57 μm in diameter (as calculated from inkjet drop volume analysis in Section 3.1) with v = 6 m/s ejection velocities [61]. Liquid–solid co-printing involves the deposition of these micro-scale droplets onto either a solid–air interface or a liquid–air interface. The solid–air interface in which multi-material inkjet droplets mix and interact has been studied extensively in Zoretto et al. and Mueller et al. and thus the focus of this work is on the liquid–air interface [62,63]. In the latter scenario, the interaction dynamics of a liquid droplet impacting a liquid–air interface will dictate the final print properties. Hence, we created a series of experiments to elucidate the mechanisms and mechanics of this interaction. Since the Stratasys J750 is a closed commercial system, access to install optics and a droplet-synchronized high speed camera under the printhead for micro-scale droplet imaging is infeasible. As such, a scaling analysis matching governing non-dimensional numbers for droplet impact is used to experimentally study representative droplet impact dynamics via high speed imaging at the meso-scale. Droplet impact behavior can be described by a series of dimensionless numbers which are presented below, where D is the drop diameter, ρ is the fluid density, v is the fluid velocity, γ is the surface tension, μ is the dynamic viscosity, and g is the acceleration due to gravity. Specifically, the Weber (We), Reynolds (Re), Ohnesorge (Oh), and Bond (Bo) numbers describe drop impact dynamics [64–67]. Using the aforementioned micro-scale drop diameter and ejection velocity along with each resin's fluid properties, the range of governing non-dimensional numbers at the micro-scale are: We = 50–70, Oh = 1–3, Re = 2.5–5.0, and Bo = 10^{-4}-10^{-3}. To ensure physics similarity, drop diameters and velocities on the *meso-scale* were selected such that the Weber, Ohnesorge, and Reynolds numbers governing drop impact were within one order of magnitude to that of the micro-scale. CFD models were then validated from the experimental scaling analysis study (described in Section 6.4) and applied to study the fluid dynamics of photo-resin drop impacts on an immiscible liquid surface at the micro-scale.

Dimensionless Number	Physical Meaning	Definition
Weber Number	Ratio of inertial to surface tension forces	$We = \frac{\rho v^2 D}{\gamma}$
Ohnesorge Number	Ratio of viscous to inertial and surface tension forces	$Oh = \frac{\mu}{\sqrt{\rho \gamma D}}$
Bond Number	Ratio of gravitational to surface tension forces	$Bo = \frac{\rho g D^2}{\gamma}$
Reynolds Number	Ratio of inertial to viscous forces	$Re = \frac{\rho v D}{\mu}$

2.2.1. Meso-scale drop impact case studies

Single Drop Impact, Same Fluids

CFD models are first validated for the 2-phase flow case in which a drop of non-solidifying fluid impacts a reservoir of the same fluid. Figure 2a and movie S1 illustrate a D = 2.89 mm drop of non-solidifying liquid impacting a H = 5 mm non-solidifying liquid reservoir at v = 0.833 m/s. Drop dynamics were recorded at 5000 fps using a Phantom V710 high speed camera according to the setup described

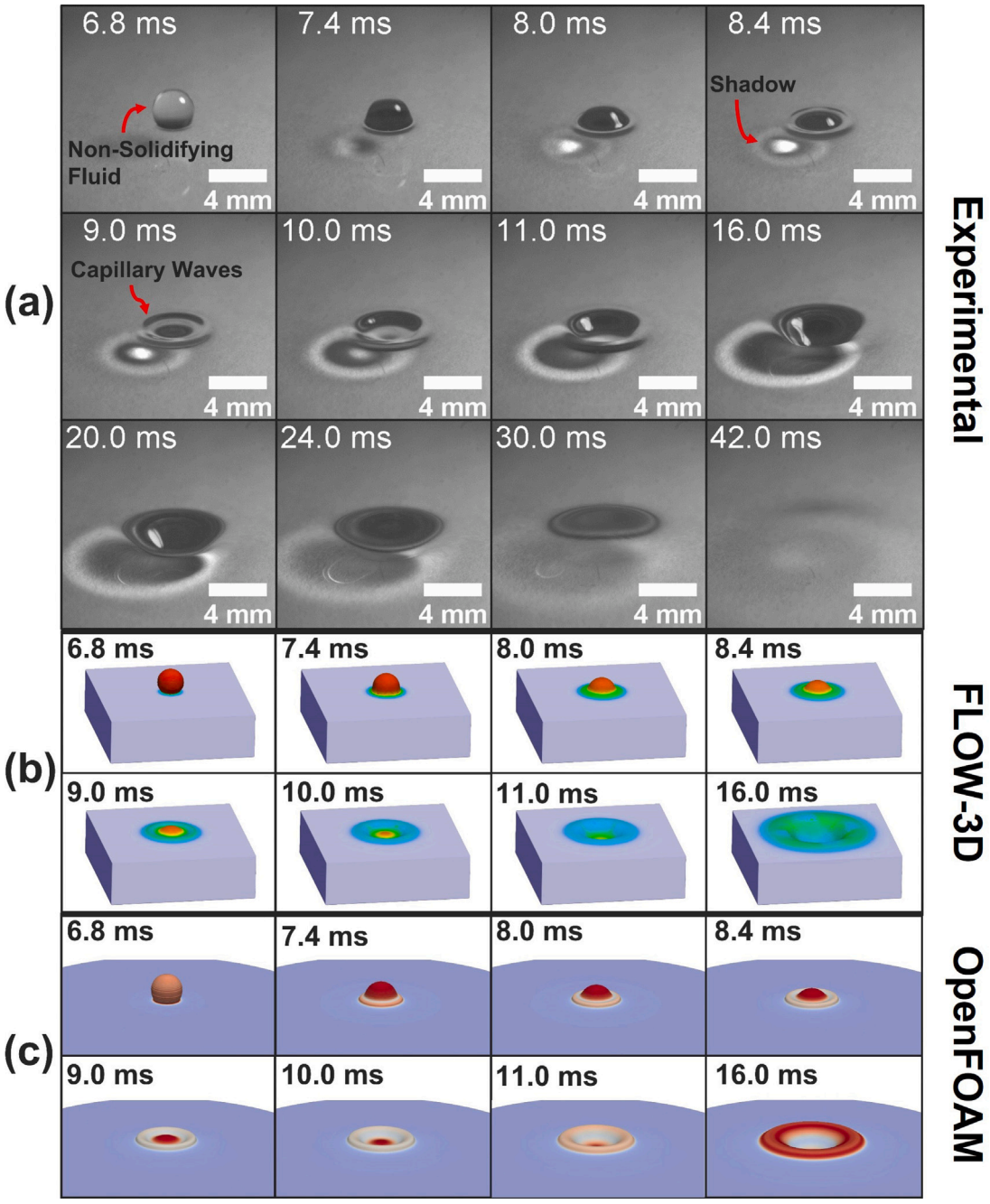

Fig. 2. Liquid–Solid Co-Printing Mechanism Non-Solidifying Fluid Impact — time lapse of a D = 2.89 mm drop of non-solidifying liquid impacting a H = 5 mm reservoir of non-solidifying liquid at v = 0.833 m/s. (a) shows experimental high speed imaging, (b) shows FLOW-3D simulation of drop impact, and (c) shows OpenFOAM simulation of drop impact. Drop impact is followed by spreading due to impact kinetic energy. Capillary waves on the fluid surface dissipate the droplet kinetic energy. Low Weber number (We < 1000) and high viscosity are indicative of drop impact without crown and jet formation. Dimensionless quantities for the impact are: Re = 34.6, We = 49.2, Oh = 0.202, and Bo = 2.01.

in Section 6.4. Both FLOW-3D and OpenFOAM validation simulations matched drop size, drop velocity, and reservoir height used in the experimental study. In FLOW-3D, an 8 mm × 8 mm x 5.7 mm domain with a structured mesh of cell size 100 μm was used to simulate drop impact (Fig. 2b); in OpenFOAM, a 5° axisymmetric wedge with 400 × 400 mesh elements across a 15 mm × 8 mm domain was used to simulate drop impact (Fig. 2c). Shown in Fig. 2a–c, the liquid drop hits the liquid surface and creates a crater in the non-solidifying liquid reservoir. The drop flattens due to its kinetic energy on impact and creates capillary waves that propagate outwards from the drop impact site. Capillary waves are damped by fluid viscosity, and the liquid interface's surface tension eventually brings the interface back to its rest state 35.2 ms after impact. Dimensionless quantities for the impact are: Re = 34.6, We = 49.2, Oh = 0.202, and Bo = 2.01. Low Weber number (We < 1000) and high viscosity are indicative of drop impact without crown and jet formation [68]. In Fig. 2b–c, both FLOW-3D and OpenFOAM CFD simulated drop dynamics agree with the experimental drop impact dynamics time lapse in (a).

Single Drop Impact, Dissimilar Fluids

After validation of the 2-phase flow case, CFD models were next validated for the 3-phase flow case in which a photo-curable fluid droplet impacts a dissimilar non-solidifying fluid reservoir. Figure 3a and movie S2 illustrate a D = 2.79 mm drop of VeroCyan impacting a H = 5 mm non-solidifying liquid reservoir at v = 1.106 m/s.

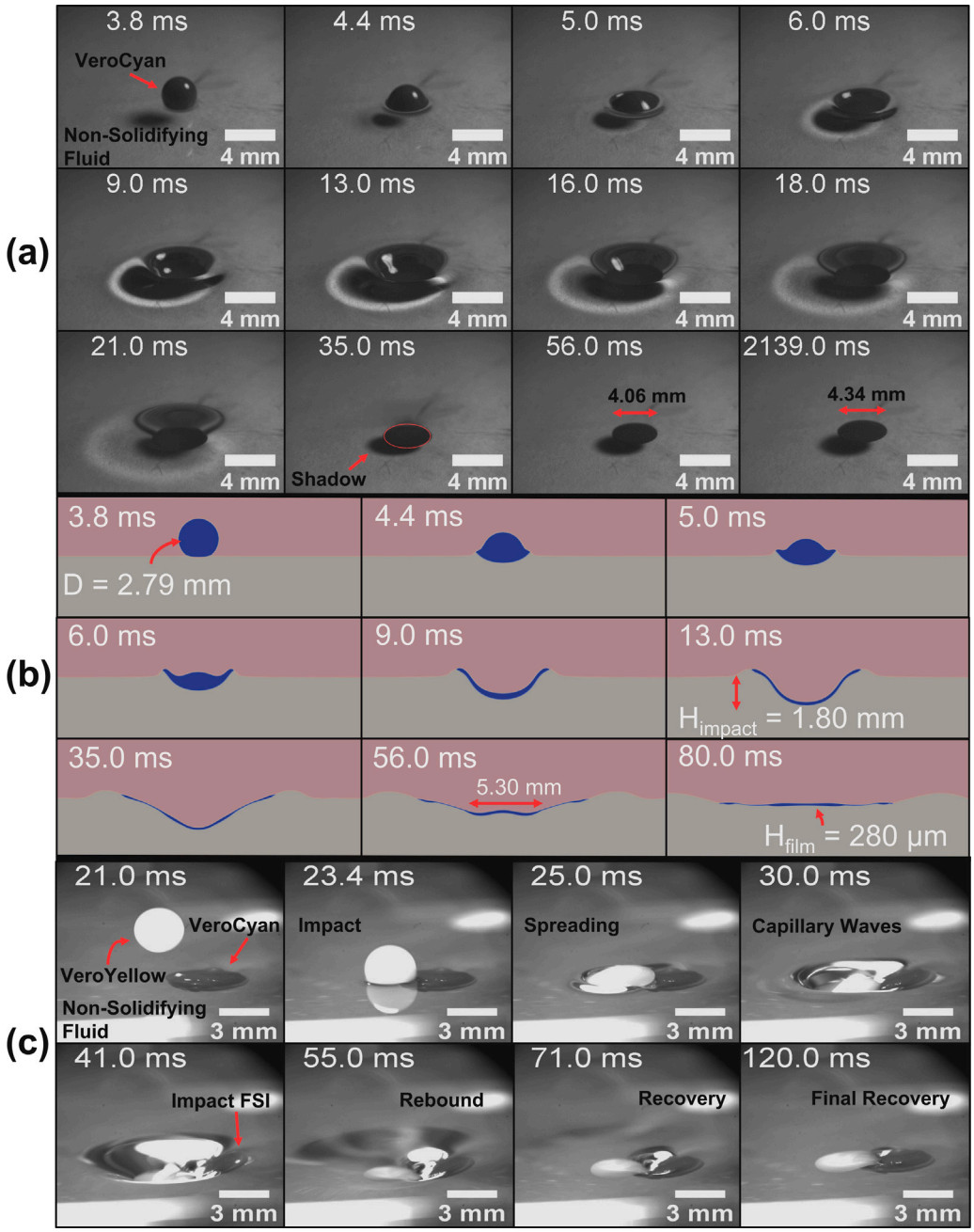

Fig. 3. Liquid–Solid Co-Printing Mechanism Single Resin and Multi-Material — (a) shows experimental high speed imaging time lapse of a D = 2.79 mm drop of VeroCyan impacting a H = 5 mm reservoir of non-solidifying liquid at v = 1.106 m/s. Drop impact is followed by spreading due to impact kinetic energy and a positive spreading factor. Resin is considered immiscible with non-solidifying liquid. Capillary waves on the fluid surface dissipate the resin droplet kinetic energy. Maximal VeroCyan droplet spreading occurred at t = 56.0 ms (52.2 ms after impact) with a length of 4.06 mm. Further droplet spreading from t = 56 ms to 2139 ms is highlighted. (b) shows OpenFOAM simulation of drop impact. The maximum impact crater occurred at t = 13.0 ms (9.2 ms after impact) at a depth of 1.80 mm. Maximal VeroCyan droplet spreading occurs at t = 56.0 ms (52.2 ms after impact) with a length of 5.30 mm. Film thickness was 280 µm after spreading. Dimensionless quantities for the impact are: Re = 23.2, We = 117.5, Oh = 0.466, and Bo = 2.63. (c) shows time lapse of a D = 3.03 mm drop of VeroYellow impacting a H=5 mm reservoir of non-solidifying liquid at v = 1.068 m/s. Drop impact is aligned over the surface of a photo-polymerized drop of VeroCyan. Fluid–structure interaction (FSI) between non photo-polymerized VeroYellow and photo-polymerized VeroCyan droplets can be seen.

Drop dynamics were recorded at 5000 fps. As before, the OpenFOAM validation simulation matched experimental drop size, drop velocity, and reservoir height and used a 5° axisymmetric wedge with 400 × 400 mesh elements across a 15 mm × 8 mm domain. Figure 3b depicts OpenFOAM simulated drop dynamics. Shown in 3a–b, the liquid VeroCyan resin drop hits the fluid surface and creates a crater in the non-solidifying liquid reservoir. The drop flattens due to its kinetic energy on impact and spreads due to a positive spreading factor [69]. The spreading factor is given by $S = \sigma_{fluid-air} - (\sigma_{resin-air} + \sigma_{fluid-resin})$ = 44.19 - (33.10 + 3.29) = 7.80 dyne/cm. A positive spreading factor indicates that the resin droplet will wet the non-solidifying liquid film and spread out on its surface [64]. After impact, capillary waves propagate outwards from the drop impact site. The maximum impact crater occurred at t = 13.0 ms (9.2 ms after impact) at a depth of 1.80 mm. Maximal VeroCyan droplet spreading occurred at t = 56 ms (52.2 ms after impact) with a length of 4.06 mm. Film thickness was 280 µm after spreading. Dimensionless quantities for the impact are: Re = 23.2, We = 117.5, Oh = 0.466, and Bo = 2.63. Similar to the same fluids case, the high viscosity of VeroCyan resin and low Weber number

(We < 1000) prevent crown and jet formation after impact. In Fig. 3a–b, OpenFOAM CFD modeling agrees with the experimental drop impact dynamics time lapse shown in (a).

Multi-Material Drop Impact, Dissimilar Fluids, Mechanism

Liquid–solid co-printing typically involves multi-material drop impacts on a liquid surface upon which cured resin has recently been deposited. To study this case, a D = 2.79 mm drop of VeroCyan was first deposited and polymerized on a H = 5 mm non-solidifying liquid reservoir. Then, as shown in Fig. 3c and movie S3, a D = 3.03 mm drop of VeroYellow is deposited at v = 1.068 m/s such that it partially impacts the polymerized VeroCyan drop floating on the fluid surface. Drop dynamics were recorded at 5000 fps. Prior to impact, it is clear that the polymerized VeroCyan drop is held on the surface of the non-solidifying liquid. This effect can be explained by a force balance between the surface tension (F_{st}), buoyancy (F_b), and drop weight forces (F_g) as described below

$$m_{drop}\ddot{z}(t) = F_{st} + F_b - F_g \tag{10}$$

where m_{drop} is the mass of the VeroCyan droplet and z(t) is the z-position of the droplet with reference to the liquid surface. Since the VeroCyan droplet rests on the liquid surface, $\Sigma F_i >= 0$. Consider a first-order approximation for each force.

$$F_{st} = 2\gamma L_c sin(\theta) \approx 1.85 \times 10^{-4}\ [N] \tag{11}$$

$$F_b = \rho_f V_{disp} g \approx 1.21 \times 10^{-4}\ [N] \tag{12}$$

$$F_g = \rho_d V_d g \approx 1.30 \times 10^{-4}\ [N] \tag{13}$$

where L_c is the length of the region in contact with the liquid surface (approximated as the droplet diameter), θ is the angle of contact the droplet makes with the liquid surface (approximated at its max when θ = 90 °), ρ_f is the non-solidifying liquid density, ρ_d is the VeroCyan droplet density, V_d is the droplet volume, and V_{disp} is the displaced volume of fluid by the VeroCyan droplet (at max buoyancy force, $V_{disp} = V_d$). Since the polymerized density of VeroCyan is greater than that of the non-solidifying liquid (see table S2), the net force resulting from buoyancy and gravity should cause the VeroCyan droplet to sink; however, it is clear from Fig. 3c that the VeroCyan droplet floats on the liquid surface. Additionally, first order approximations of the force balance results in the surface tension force being sufficient to hold up the droplet of VeroCyan; namely, $F_{st} = 1.85 \times 10^{-4} > F_g - F_b = 9.00 \times 10^{-6}\ [N]$. Thus, the photo-polymerized drop of VeroCyan is held up by the surface tension force. In general, there exist four force balance cases for liquid–solid co-printing: (1) the photo-resin is less dense than the non-solidifying liquid and the surface tension force is significant in which $F_b - F_g > 0$ and $F_s > 0$ meaning that *both* the buoyancy force and surface tension force support the photo-resin droplet, (2) the photo-resin is less dense than the non-solidifying liquid and the surface tension force is negligible in which $F_b - F_g > 0$ and $F_s \approx 0$ meaning that *only* the buoyancy force supports the photo-resin droplet, (3) the photo-resin is more dense than the non-solidifying liquid and the surface tension force is significant in which $F_b - F_g < 0$ and $F_s > 0$ meaning that *only* the surface tension force supports the photo-resin droplet, and (4) the photo-resin is more dense than the non-solidifying liquid and the surface tension force is negligible in which $F_b - F_g < 0$ and $F_s \approx 0$. Scenarios 1 or 2 are preferred for liquid–solid co-printing, as free floating structures can be created; however, Stratasys photo-resins have material properties such that scenario 3 is realized (table S2). Here, surface tension can hold up a certain mass of cured photo-resin before which its weight will cause the structure to sink. Scenario 3 is complicated by the fact that the surface tension force will vary during a print due to deformations of the liquid surface during successive inkjet droplet impacts, print bed vibrations, and roller motion. Therefore, to ensure that photo-resin droplets rest on a liquid surface, anchoring points to the surrounding solid matrix should be included (as is done naturally during the capping layer of a micro/milli-channel). Specifically, anchoring points are regions of solidifying material that attach an otherwise free-floating region of solidifying material to a larger region of stationary (anchored to the build plate) solid material in order to prevent it from moving during printing (which would cause geometry issues). We hypothesize that scenario 4 can also be realized with liquid–solid co-printing, provided that anchoring points to the surrounding solid matrix are used, because newly deposited droplets should sink slowly relative to the deposition and photopolymerization rate.

With regard to the impact dynamics in Fig. 3c, the VeroYellow droplet spreads out upon impact due to its kinetic energy and a positive spreading factor. Capillary waves propagate outwards from the drop impact site. Fluid–structure interaction between the VeroYellow liquid drop and polymerized VeroCyan solid can be seen at t = 41 ms in Fig. 3c. The VeroYellow drop spreads out partially over the polymerized VeroCyan solid during impact, resulting in a connected multi-material polymerized region which can be seen during the rebound and recovery phases. Dimensionless quantities for the impact are: Re = 24.4, We = 119.1, Oh = 0.447, and Bo = 3.11.

2.2.2. Material jetting micro-scale simulation cases

Once validated via meso-scale experiments, OpenFOAM simulations were utilized to examine micro-scale droplet impact dynamics between 2-phase and 3-phase drop impacts. A 5 ° axisymmetric wedge with 400 × 400 mesh elements across a 400 μm x 350 um domain was used to resolve liquid interfaces. In Fig. 4, OpenFOAM simulations of (a) D = 57 μm inkjet non-solidifying liquid drop impacting a H = 200 μm non-solidifying liquid reservoir, and (b) D = 57 μm inkjet VeroCyan drop impacting a H = 200 μm non-solidifying liquid reservoir are shown. Drop velocities were estimated from literature as v = 6 m/s [61] and drop diameter was estimated from experimental data discussed in 3.1. Illustrated in Fig. 4a, the non-solidifying liquid inkjet drop exhibits the same impact dynamics as observed on the meso-scale but at a faster time scale. Here, the maximal crater depth occurred at t = 75 μs (60 μs after impact) with a crater depth of 30 μm. Non-solidifying liquid interface recovery takes approximately 1000 μs after drop impact. Additionally, a perfect perpendicular impact can be seen to trap air in the liquid which agrees with the literature [70]. Dimensionless quantities for the impact are: Re = 4.91, We = 50.33, Oh = 1.44, and Bo = 7.82 × 10^{-4}. Similarly, Fig. 4b illustrates the same drop impact dynamics of VeroCyan on non-solidifying liquid as seen on the meso-scale but at a faster time scale. The VeroCyan drop initially spreads out after impact due to its kinetic energy and a positive spreading factor as the VeroCyan liquid can be seen to wet the non-solidifying liquid surface. The maximal crater depth is reached at t = 90 μs (75 μs after impact) and is 37 μm below the liquid interface. After approximately 485 μs (t = 500 μs), the VeroCyan drop fully spreads out and wets the non-solidifying liquid surface to a length of 143 μm. The film thickness was 5 μm after spreading. As can be seen in Fig. 4, drop impact substantially deforms the non-solidifying liquid interface from which it takes longer than 1000 μs to recover. Dimensionless quantities for the impact are: Re = 2.57, We = 70.4, Oh = 3.26, and Bo = 1.09 × 10^{-3}.

Next, we extend single micro-scale droplet simulations to the capping layer involving hundreds of photo-resin droplet impacts. Here, a 1 mm × 1 mm × 216 μm non-solidifying fluid region surrounded by a solid matrix is impacted by a VeroCyan droplet array sequence spaced according to the J750 print resolution (600 dpi in the x-direction and 300 dpi in the y-direction). The printhead z-offset from the print bed was measured to be 1.60 mm. The printhead velocity was determined from feature tracking in high speed image analysis to be 502.1 ± 7.4 mm/s (Fig. 5a–b). The first pass of the capping layer was simulated using a 3 μm structured grid requiring approximately 22,000,000 mesh elements and 9,600 core hours. As can be seen in Fig. 5c–e and movie S4, the VeroCyan droplet array sequence impacts create an advancing capillary wave in the direction of printhead motion. The capillary wave is 176 μm above the initial liquid surface level and spills over the solid matrix, likely influencing the curing of photo-resin immediately surrounding the liquid region. Indeed, we

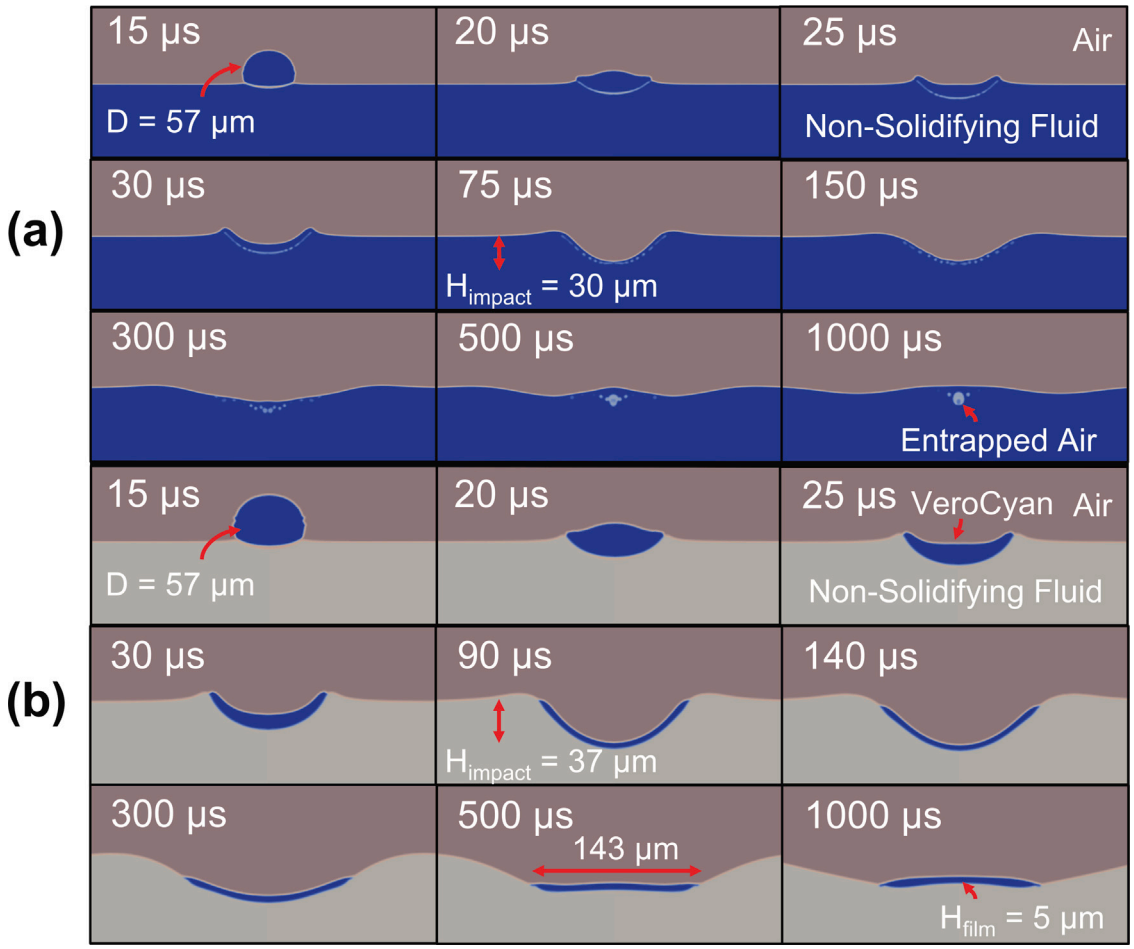

Fig. 4. Liquid–Solid Co-Printing Mechanism Simulation at the Micro-Scale — OpenFOAM simulation time lapse of a D = 57 µm drop of non-solidifying liquid and VeroCyan resin, (a) and (b) respectively, impacting a H = 200 µm reservoir of non-solidifying liquid at v = 6 m/s. (a) non-solidifying liquid drop impact is followed by spreading due to its kinetic energy. Capillary waves from impact are dissipated by viscosity. The maximum impact crater occurred at t = 75 µs (60 µs after impact) at a depth of 30 µm. Dimensionless quantities for the impact are: Re = 4.91, We = 50.3, Oh = 1.44, and Bo = 7.82×10^{-4}. (b) VeroCyan drop impact is followed by spreading due to its kinetic energy and a positive spreading factor. Resin is considered immiscible with non-solidifying liquid. Capillary waves from impact are dissipated by viscosity. The maximum impact crater occurred at t = 90 µs (75 µs after impact) at a depth of 37 µm. After approximately 485 µs, the VeroCyan drop fully spreads out and wets the non-solidifying liquid surface to a length of 143 µm. Film thickness was 5 µm after spreading. Dimensionless quantities for the impact are: Re = 2.57, We = 70.4, Oh = 3.26, and Bo = 1.09×10^{-3}.

observe experimentally that bonding between subsequent layers of the photopolymer adjacent to a liquid region is inhibited when excess liquid is present. We also note the existence of non-cured resin ridges in Fig. 5e. Such resin ridges form due to fluidic interactions of the droplet array sequence and the liquid surface upon successive impact events. We hypothesize that these resin ridges are cured on the liquid surface at the conclusion of the first capping layer which corresponds with features seen from the experimental capping layer analysis in Fig. 11. Figure 5f–h shows the 2D cross-section for each time segment to illustrate the capillary wave evolution. It is to be noted that air entrapment occurs during the simulated capping layer print process *without* the roller engaged, resulting in potential surface defects consistent with the experimental analysis in Fig. 11.

3. Print process characterization

3.1. Liquid voltage level analysis

Material jetting 3D printers build an object from the bottom-up, layer-by-layer, by depositing droplets of material. Each of these droplets can be approximated as a voxel (volumetric pixel) and the entire design is described by assigning a material type to every available voxel location in the design. In the Stratasys J750 system, the fabrication resolution is 600 (X) × 300 (Y) × 940 (Z) dots per inch, which implies a voxel size of 42 × 84 × 27 µm. The J750 head voltage can be adjusted to control the volume of each droplet deposited, which allows inks to be underjetted or overjetted (relative to the voxel volume), thereby changing the volume-filled in each voxel location. To characterize the volume of liquid jetted as a function of head voltage, liquid "boats", as depicted in Fig. 1, were printed and the liquid height was measured via calipers and a Keyence VK optical profilometer to estimate the jetted liquid volume. To make manual caliper measurements, the height of the liquid region must be large enough to accurately measure. In this study, the caliper analysis used liquid boats with a liquid region of 12 mm × 12 mm × 14 mm. The optical profilometer approach used liquid boats with a liquid region of 40 mm × 40 mm × 2 mm as the Keyence VK z-resolution was 16 µm. To normalize different liquid regions, the volume of liquid printed *per voxel* is reported. Furthermore, the Stratasys J750 can accept design files described by surface-boundary triangles (STL) or voxels. In either case, the printer deposits material droplets into voxel locations in the build region, making the volume of liquid printed per voxel a natural design parameter. Since the print resolution is known, the number of voxels in the STL liquid boat design can be estimated whereas it is exactly known in the voxel mode liquid boat design.

Liquid boat designs provide a good estimate of the printed liquid volume per voxel up until the point at which overjetting occurs. Beyond this point, the integrated roller removes excess jetted liquid which results in a horizontal asymptote at the maximum liquid volume per voxel

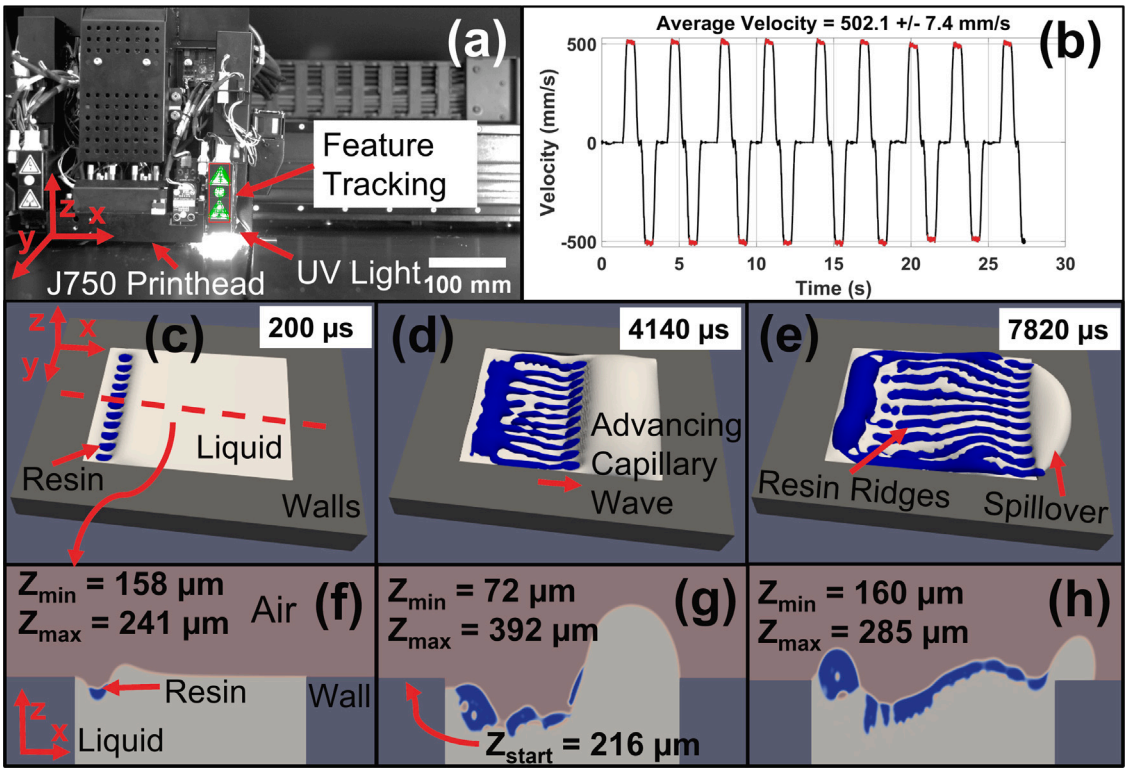

Fig. 5. Capping Layer Simulation at the Micro-Scale — OpenFOAM simulation of a 1 × 1 mm^2 capping layer. (a) illustrates tracking of the J750 printhead to extract printhead velocity for the simulation. (b) shows the printhead velocity for 9 passes with an average velocity of 502.1 ± 7.4 mm/s. (c-h) show VeroCyan droplet array sequence impact (D = 57 µm) with the non-solidifying liquid surface interface at H = 216 µm. Each droplet is spaced according to the J750 print resolution of 600 dpi in the ×-direction and 300 dpi in the y-direction. Droplets are ejected from all nozzles simultaneously in an "array sequence", and this sequence is repeated every 42 µm. Drop velocity is $\mathbf{v} = [v_x, v_y, v_z]$ where v_x is the printhead velocity, v_y = 0 m/s, and v_z = -6 m/s. Droplet array sequence impact creates a propagating capillary wave in the direction of printhead motion (d) which spills over the surrounding sidewalls (e). Droplet array sequence impact occurs on the advancing capillary wave causing droplets to slide down the liquid and coalesce. Additionally, resin ridges can be seen in (d–e) which are observed experimentally. (f–h) show a 2D cross-section at each time segment and depicts the minimum and maximum non-solidifying liquid z-height. Air entrapment can be seen in (g–h).

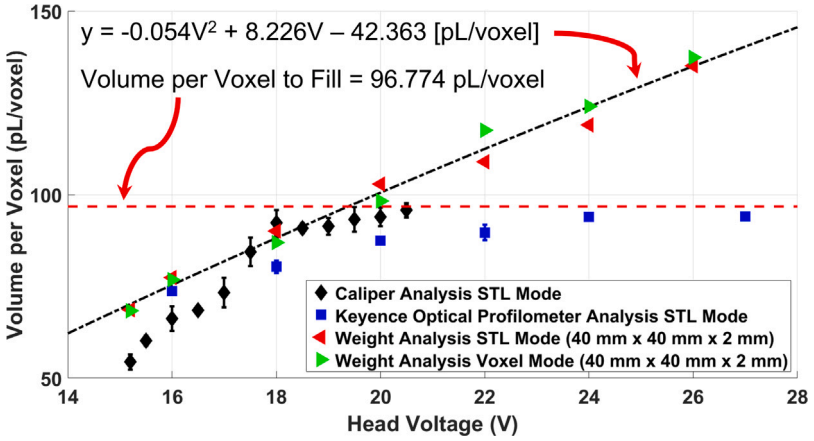

Fig. 6. Liquid Voltage Level Analysis — illustrates how the amount of liquid jetted varies as a function of the head control voltage. Three different measurement methods were compared to estimate the printed liquid volume per voxel: (1) manual caliper measurement of the liquid height, (2) keyence optical profilometer analysis of the liquid height, and (3) direct liquid weight analysis. The liquid weight analysis is the best estimate for the printed liquid volume per voxel and it was determined that the head voltage required to obtain the volume per voxel to completely fill the liquid boat is 19.38 V. Both STL and voxel print modes resulted in nearly the same printed liquid volume per voxel. The red horizontal dashed line shows the theoretical volume per voxel, based on the advertised print resolution. The black dash-dot line shows a second order polynomial fit to the weight analysis data where y is the volume per voxel in pL/voxel and V is the head voltage. Each sample point was performed in triplicate.

to fill the liquid boat. In order to obtain a direct measurement of the printed liquid volume per voxel for both underjetting and overjetting voltage levels, the print bed was lowered and glass petri dishes were positioned on the print bed such that the printheads jetted directly into the glass petri dishes without the roller being in contact. The mass of jetted liquid was then converted into jetted volume using the measured fluid density (see table S2). As shown in Fig. 6, firing voltage was varied from 15.2 V to 27 V and the volume per voxel was determined through the previously discussed methods. Each measurement was performed in triplicate. The theoretical volume per voxel to fill, as defined by the printer resolution, is 96.774 pL/voxel. Figure 6 shows that the caliper and Keyence optical profilometer analysis reach a horizontal asymptote at the theoretical volume per voxel to fill level. This is due to the roller removing excess liquid in Stratasys J750 systems. When the print bed is

lowered and material is directly jetted into petri dishes for the weight analysis method, the roller is not in contact and thus a true volume per voxel as a function of voltage is obtained. Using the second order polynomial fit, the theoretical volume per voxel to fill level is reached at 19.38 V. It is desired to underjet liquid to avoid liquid spilling over the wall edges and interaction with the integrated roller, which would cause contamination of adjacent solid regions. Therefore, a head voltage of 19 V in the liquid channel was used for all experiments and figures in this study (unless otherwise indicated) to ensure underjetting of liquid.

3.2. Capping print layer analysis

The capping print layer, from a multi-physics viewpoint, is the most complex component of liquid–solid co-printing. Hundreds of thousands of photo-resin droplets (which can be different materials) are deposited on a liquid interface and photo-polymerized all while a roller moves across the liquid interface. In this study, the capping print layer was characterized by printing boats containing liquid, on top of which capping layers consisting of 1, 2, 3, or 5 layers of photo-resin were printed as shown in Fig. 11. Boats were printed in both STL and voxel modes, but no differences between the two print modes were observed and thus we showcase only the STL mode in Fig. 11 for brevity. To assess the impact of the roller on the capping layer, boats were printed both with the roller engaged and with the roller raised by 500 μm to ensure no contact with the print layers. As illustrated in Fig. 11, after 5 print layers, the liquid surface is fully encapsulated by cured solid photo-resin. Figure 11a–d shows the encapsulation of the liquid as a function of print layer when the roller is engaged while Fig. 11e–h shows encapsulation when the roller is indexed up by 500 μm and no longer in contact with the print. In Fig. 11h, air entrapment is observed when the roller is indexed up which is consistent with simulations. Figure 11g–h shows additional fluid buildup on the capping layer surface when the roller is raised which is consistent with the fact that the roller is not removing excess liquid material; we note that the liquid encapsulation is nearly identical when the roller is engaged or indexed up. In both instances, the first capping print layer creates lines of polymerized resin in the direction of the printhead motion. We hypothesize that these polymerized resin lines are due to interacting capillary waves in the liquid during impact of the hundreds of thousands of droplets on the liquid surface which creates a standing wave effect of peaks and troughs, leading to local photopolymer material accumulation during polymerization. These photo-polymer ridges are consistent with x-ray microscopy (XRM) imaging of the top channel wall in Section 3.4 as well as CFD simulations of the capping layer (Fig. 5) and result in an increased channel surface roughness. In Fig. 11i-l, multi-material print capabilities during the capping layer are demonstrated by printing a multi-material University of Colorado Boulder (CU) buffalo directly on top of a liquid-phase support material. Additionally, it is demonstrated that the cured photo-resin (which is more dense than the non-solidifying liquid) can be supported on the surface of the liquid through the use of attachment points to a solid region as shown by the VeroMagenta attachment points for the CU Boulder buffalo logo. While surface tension alone can theoretically support cured photo-resin droplets of density greater than that of the support liquid, liquid surface deformations due to the roller and droplet impacts can reduce the surface tension force causing photo-polymerized droplets to sink. Thus, it is best practice to use attachment points to the solid matrix where possible to ensure support of cured photo-resin layers.

3.3. Effect of the integrated roller

Most commercial material jetting 3D printers have a leveling mechanism that moves across the print area to ensure a planar surface during a print. In Stratasys PolyJet and 3D Systems Multi-Jet printers, an integrated metal cylinder (the "roller") with a driven axis of rotation parallel to the build surface is used to level the part. Since the roller can be in contact with the liquid surface, it plays an important role in liquid–solid co-printing. When the roller contacts a liquid surface, it drags liquid into the polymer matrix resulting in a phenomenon we term *liquid fingers*. Such an effect is undesirable as it introduces potential leakage pathways and increases the necessary channel pitch to ensure fluidically isolated channels. Figure 7 shows that liquid fingers result from overjetting. Specifically, an enclosed helical channel (r = 500 μm) wrapping around a central circular channel (r = 500 μm) was printed using a firing voltage of 19 and 24 V to underjet and overjet liquid respectively. Rhodamine B dye was flowed through the helical channel to allow fluorescent imaging. A Nikon TiE inverted spinning disk confocal fluorescent microscope was then used to optically cross-section the mid-point of the helical channel. Figure 7a–b illustrate that liquid fingers do *not* form when liquid is underjetted whereas Fig. 7c–d illustrate that liquid fingers do form when liquid is overjetted. When liquid is underjetted, the volume of liquid deposited on each print layer is such that liquid does *not* come in contact with the roller; in contrast, when liquid is overjetted, the volume of liquid deposited on each print layer is such that liquid *does* contact the roller which then drags liquid into the polymer matrix. Liquid fingers are on the size order of 300 μm for a circular channel of radius 500 μm. We note that indexing the roller up (see [33] for instructions on how to access the motor controller) so it is not in contact with the part is a way to eliminate the liquid finger phenomenon even when overjetting; however, the roller is important to ensure part dimensionality on the Stratasys J750 and raising the roller would be ill-suited for parts with a total height larger than a few millimeters. Thus, it is desired to *underjet* liquid with the roller in contact, as done in this work, in order to avoid creating liquid fingers around channels.

3.4. Micro/milli-fluidic wall characteristics

Wall characteristics are important for micro/milli-fluidic channels as a low surface roughness is useful for device repeatability and optical transparency while a high surface roughness can enhance laminar mixing [71]. Figure 12 shows bottom, top, and side wall characteristics of a 3 mm × 3 mm milli-channel with an internal, hanging beam containing a D = 500 μm bore along its base. The channel is made of VeroClear while the internal, hanging beam is made of flexible TangoBlack+. A Zeiss Xradia 520 Versa X-ray Microscope (XRM) was used to inspect the milli-channel walls via micro-computed tomography (micro-CT).

Before addressing the wall characteristics, we note the ability of liquid–solid co-printing to fabricate internal, hanging structures using the liquid interface as a support material. This geometry would be infeasible without liquid support and contains several distinct regions where photopolymer was supported by noncuring liquid. With respect to the wall characteristics, Fig. 12 shows three unique wall surfaces: (a) smooth bottom wall, (b) non-ordered ridges on sidewalls, and (c) ordered ridges on top wall. Primarily, the smooth bottom wall is due to the roller smoothing deposited photo-resin droplets. This creates a uniform and smooth channel surface on the bottom wall. As the channel is built in the z-direction, the left and right sidewalls are modified during each pass. Upon reaching the capping layer, ordered polymer ridges form on the liquid surface aligned with the printhead direction of motion. Both the sidewalls and top wall possessed a maximal surface peak roughness height of approximately $S_z = 150$ μm while the bottom surface possessed a maximum surface peak roughness height of $S_z \leq 4.6$ μm since the XRM scan resolution was 4.6 μm and no discernible surface roughness was observed.

3.5. Minimum repeatable channel print resolution

For any micro/mesofluidic fabrication technique, the minimum repeatable channel resolution is a key design parameter. Minimum repeatable channel print resolution was assessed as a function of channel

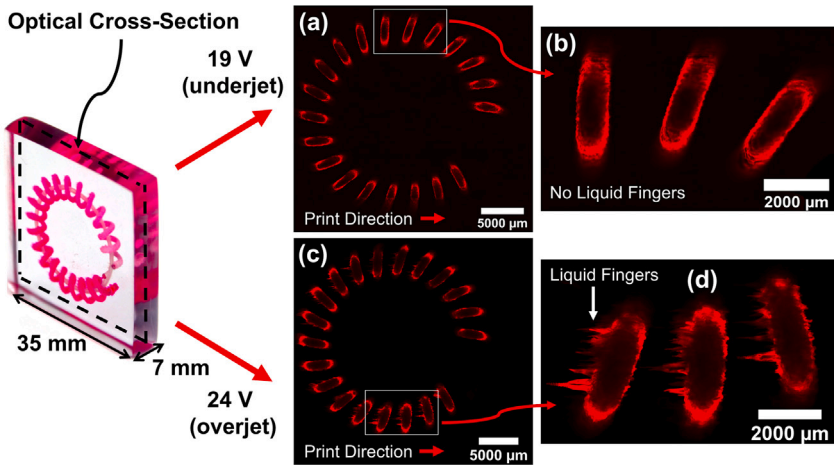

Fig. 7. Effect of Voltage on Print Quality — depicts the impact of depositing more or less liquid material. An enclosed helical channel (r = 500 μm) wrapping around a central circular channel (r = 500 μm) was printed and post-processed in 1 h in both the underjetting (19 V) and overjetting (24 V) firing voltage conditions. The leveling mechanism (roller) interacts with jetted material, moving it away from the deposition region. These streaks of transported liquid material modify the intended geometry; we call them "liquid fingers" due to their characteristic shape. (a–d) show optical fluorescent cross-sections after staining with rhodamine B dye. (a–b) show no liquid fingers because liquid is underjetted at each print layer and does *not* come into contact with the roller, while (c–d) show liquid fingers because liquid is overjetted at each print layer and the roller drags excess liquid into the polymer matrix.

orientation (perpendicular, parallel, and 45° to the printhead direction of motion) by printing 3 sample replicates of channels of width 500, 400, 250, 200, and 100 μm for each of the following channel heights which are integer multiples of the z print resolution: 486, 351, 270, 216, 162, 108, 81, and 27 μm. Channels were cross-sectioned in accordance with the method described in Section 6.2. Figure 13a depicts the part placement orientation on the print bed. Figure 13b–d illustrate example cross-sectional areas of 400 μm × 81 μm, 250 μm × 81 μm, and 500 μm × 486 μm channels respectively with the computed channel cross-section boundaries highlighted in red. Figure 13e shows the dependence of the channel cross-sectional area on channel orientation with respect to the printhead direction of motion, channel width, and channel height. As the channel height decreases from H = 486 μm to H = 27 μm, the normalized measured channel cross-sectional area also decreases. This relationship holds until a design channel width of W = 200 μm, at which point channel height is uncorrelated with normalized cross-sectional area. At a design channel width of W = 200 μm, the normalized measured channel cross-sectional area remains approximately the same across design channel heights. Full cross-section data across each printed channel is displayed in table S1. It is to be noted that the channel cross-sectional area varies by an average of 5.6% along the length of a channel (computed by the average standard deviation of all the measured normalized channel cross-sectional areas). Additionally, it is observed that the actual printed channel cross-sectional areas are less than 60% of the design cross-sectional areas for channels W = 500 μm and H = 486 μm and smaller. Thus, liquid–solid co-printing allows fabrication of truly microfluidic channels but with realized channel cross-sectional areas that are smaller than the designed channel cross-sectional areas. In general, channels placed parallel to the printhead direction of motion resulted in measured cross-sections closest to the design dimensions. When placed parallel to the printhead direction of motion, the minimum repeatable channel cross-section design was 250 μm × 81 μm (W × H) which resulted in channels that are 67% smaller than the design dimensions. For channels printed 45° and perpendicular to the printhead direction of motion, the minimum repeatable design channel cross-section was 250 μm × 108 μm which resulted in channels that are 68% smaller than the design dimensions.

4. Planar, 3D, and multi-material micro/mesofluidic structures and applications

3D printed fluidic circuits are becoming increasingly relevant in soft robotics for actuation, computation, and control as well as in biomedical and chemical analysis applications, yet they require significant labor to fabricate complex designs [72–76]. As fluidic circuits expand into 3D, it becomes increasingly difficult to purge support material from complex designs such as branched channels or internal valves. Liquid–solid co-printing provides a means to accelerate the fabrication of planar and 3D fluidic circuits with integrated valves that can be printed and easily post-processed in a matter of hours.

4.1. Planar micro/mesofluidics

At its core, micro/mesofluidics enables precise manipulation of fluid. Here, we demonstrate sample micro/mesofluidic operations such as laminar flow, mixing, and droplet generation to show the ease with which planar micro/mesofluidic devices can be fabricated using liquid–solid co-printing. In Fig. 8, a 50.8 × 50.8 × 3 mm^3 planar mesofluidic device with channel cross-sections of 1 × 1 mm^2 was fabricated and post-processed in under an hour. In (1a), laminar flow is demonstrated by co-flow of water and fluorescein dye; in (2–3a), mixing of fluorescein and rhodamine B using a serpentine milli-channel is demonstrated; and, in (4–5a), droplet generation using mineral oil and water with surfynol is demonstrated. Inlet ports are composed of flexible TangoBlack+ to provide a fluidic seal. We note the ability of this print process to easily integrate rigid, flexible, and transparent materials into micro/mesofluidic device fabrication.

4.2. 3D micro/mesofluidics

For the better part of the last few decades, micro/mesofluidic circuits were planar or 2.5D devices; that is, fabrication technologies could not easily produce fully 3D devices of arbitrary shape. After the advent of 3D printing, the micro/mesofluidic community began fabricating 3D geometries previously unrealizable to further enhance control of fluidic operations [77,78]. Here, we note the ability of liquid–solid co-printing to enable rapid, simple fabrication of arbitrary *multi-material* 3D micro/mesofluidic channels. Specifically, Fig. 9 demonstrates the fabrication of sample 3D micro/mesofluidic geometries which would be arduous or near impossible to fabricate through other means. In (a), an enclosed spiral channel (r = 500 μm) wraps around a helical central channel (r = 500 μm) which was printed and post-processed in 2 hours; in (b), an enclosed spiral channel (r = 500 μm) wraps around a planar circular channel (r = 500 μm); and, in (c–d), highly tortuous mesofluidic capillary channels were easily purged with a single inlet and outlet port. The ability to fabricate complex mesofluidic capillary structures

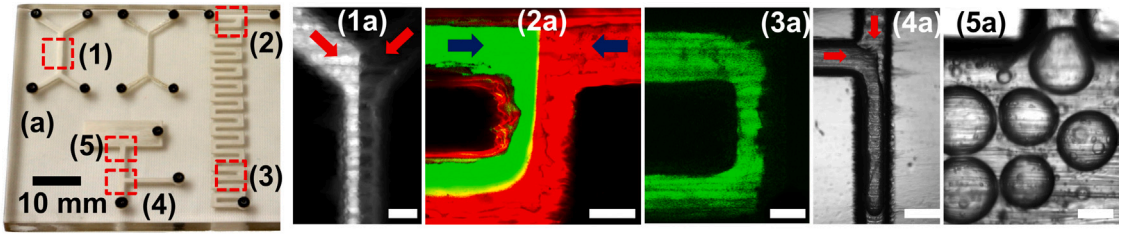

Fig. 8. Planar Micro/Mesofluidic Operations — depicts sample fluidic operations commonly performed on micro/mesofluidic devices. (a) shows a printed 50.8 × 50.8 × 3 mm^3 planar mesofluidic device with channel cross-sections of 1 × 1 mm^2 that was fabricated and post-processed in less than 1 h. (1a) illustrates laminar flow of distilled water and fluorescein, (2–3a) show laminar flow mixing of fluorescein and rhodamine B dye through a serpentine milli-channel, and (4–5a) show water/oil droplet generation with surfynol surfactant in the water phase. Millifluidic channels were printed using a head voltage of 19 V. Scale bars, 1000 μm (unless otherwise indicated).

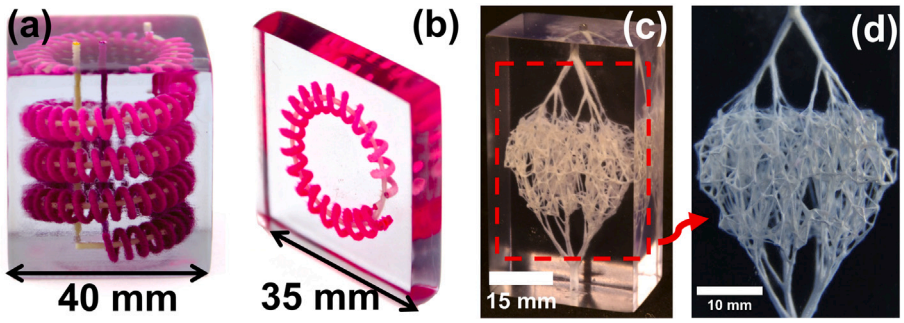

Fig. 9. 3D Micro/Mesofluidic Geometries — depicts sample 3D micro/mesofluidic geometries enabled by liquid–solid co-printing which would be previously arduous or near impossible to fabricate. (a) illustrates enclosed spiral channels (r = 500 μm) wrapping around a helical central channel (r = 500 μm) which was printed and post-processed in 2 hours. (b) illustrates enclosed spiral channels (r = 500 μm) surrounding a planar circular channel (r = 500 μm). (c–d) illustrate tortuous mesofluidic capillary channels which are easily purged with a single inlet and outlet port [images courtesy of Lawrence Smith]. The geometries were printed using a head voltage of 24 V.

demonstrates the ease in which the liquid–solid co-printing process can be used for highly complex 3D micro/mesofluidic devices which would be previously near impossible to fabricate. We anticipate liquid–solid co-printing to enable new advances the field of 3D micro/mesofluidics.

4.3. Multi-material micro/mesofluidics

The prior sections demonstrated the ability to rapidly fabricate both planar and 3D micro/mesofluidic geometries. However, a key advantage of the liquid–solid co-printing material jetting process is the ability to integrate many different materials (rigid, flexible, transparent, and now liquid) in a device, thus enabling direct fabrication of fully hydraulic systems. In Fig. 10, a one-way flap valve is demonstrated and characterized. The experimental measurement setup is described in (a) with TangoBlack+ being used for the flexible valve. The flexible valve is 500 μm thick and 200 μm above the bottom of the channel with a 500 μm offset from the side walls as described in (b). The flap valve rests over a 1 × 1 mm^2 channel opening in a 3 × 3 mm^2 channel and extends 2 mm from the end of the channel opening and 5 mm from the anchoring wall. Upon application of forward flow, the flap valve opens and flow passes through the channel; upon application of reverse flow, the flap valve closes and pressure builds in the channel. Flow is varied from 1 to 10 mL/min in the forward direction and 0.05 to 0.90 mL/min in the reverse direction. The error was determined from the transient pressure deviation from the mean at each steady-state flow rate and was at max 0.25 kPa. The exponential rise in pressure at the valving point indicates that the flap valve closes over the channel opening preventing reverse flow. We note that a fluid system using this microvalve, implemented as a print-in-place 3D part, would be extremely challenging to fabricate using conventional removable support material since mechanical removal of solidified support material would damage the flexible valve, and the valve geometry inherently creates regions with little to no flow, confounding phase-change support removal via pressure-driven purge steps. Although we demonstrate and characterize a simple flap valve, one can imagine the very-large-scale integration of hundreds of channels and valves in a soft robot. In the past, fabrication of such devices would be arduous and add substantial complexity to the entire system development; with this present work, we expect liquid–solid co-printing to enable simple and rapid fabrication of complex multi-material, 3D hydraulic systems thus enabling new advances to the field of soft robotics as well as micro/mesofluidics.

5. Discussion

The present study deals with fundamental understanding and characterization of the liquid–solid co-printing process through high speed imaging, CFD, and experimentation. The liquid–solid co-printing process was broken down into droplet–liquid interactions and liquid–wall interactions. Droplet–liquid interactions were studied at the individual droplet scale (photo-resin drop impact on a liquid surface) as well as at the system scale (capping layer involving hundreds of thousands of droplets impacting a liquid surface). It was found that in PolyJet liquid–solid co-printing with Stratasys resins, the non-solidifying liquid's surface tension supports photo-polymer droplets that photo-polymerize on the liquid surface to form a solid layer of material. In the use of any combination of working fluid and photo-resins, there are four potential governing force balance cases: (1) the photo-resin is less dense than the non-solidifying liquid and surface tension is significant, (2) the photo-resin is less dense than the non-solidifying liquid and surface tension is negligible, (3) the photo-resin is more dense than the non-solidifying liquid and surface tension is significant, and (4) the photo-resin is more dense than the non-solidifying liquid and the surface tension force is negligible. Scenarios 1 and 2 are desirable as they enable the fabrication of free floating structures; however, due to Stratasys photo-resin material properties (Table S2), PolyJet liquid–solid co-printing falls within scenario 3. Here, anchoring points with the surrounding resin are used to ensure photo-resin drops rest on the liquid surface. We hypothesize that scenario 4 can be realized so long as anchoring points are utilized which will be the focus of future work. On the system scale, approximately 5 print layers (135 μm) were required

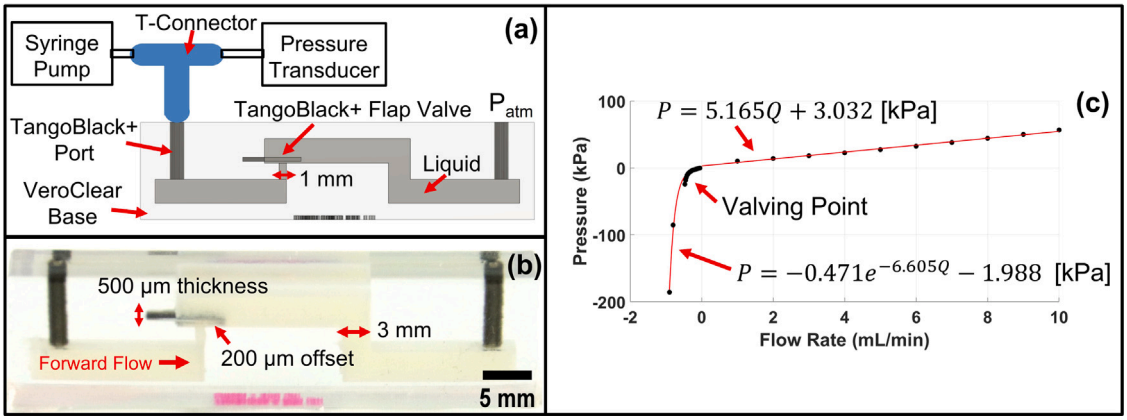

Fig. 10. Multi-Material Flap Valve — depicts an example of integrating rigid, flexible, transparent, and liquid materials to create a fully integrated flap valve in-situ with the print process. (a–c) show fabrication of a multi-material flap valve which was printed and post-processed in 30 min. (a) shows a 2D cross-section of the flap valve design along with the experimental setup. (b) shows the 3D printed multi-material flap valve device. The flap valve covers a 1 × 1 mm^2 channel opening and is 500 μm from the channel walls, 500 μm thick, and 200 μm above the bottom of the channel. (c) depicts the flap valve forward and reverse direction pressure versus flow rate characterization. The maximum error is 0.25 kPa. Curve fits are included where P is the pressure in kPa and Q is the flow rate in mL/min. A head voltage of 19 V was used to print the device.

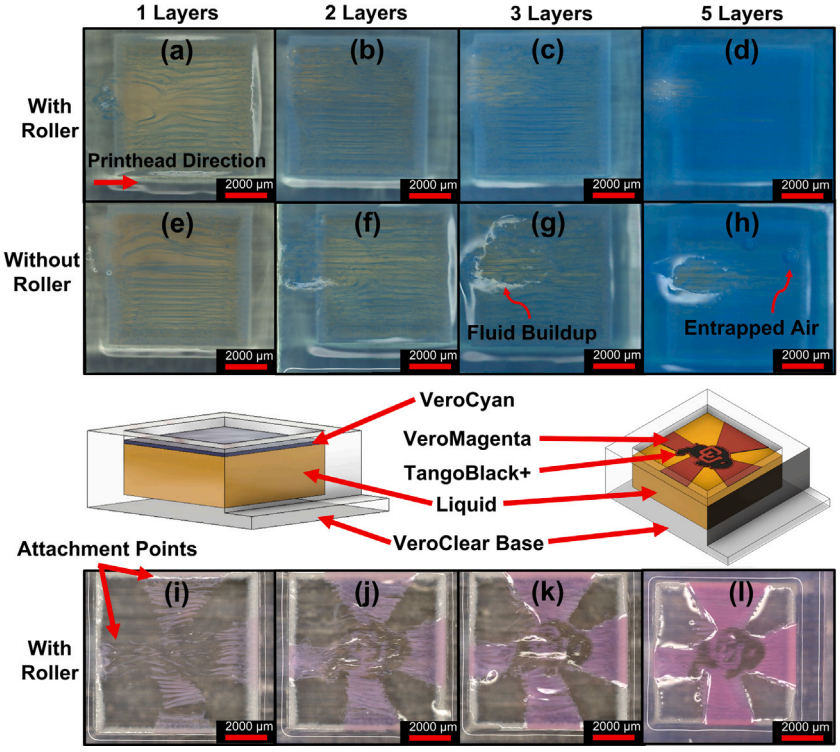

Fig. 11. Capping Layer Interface Evolution — depicts the solid/liquid interface formation as a function of the number of printed capping solid layers with and without the roller in STL mode. Each capping layer is 27 μm. (a–d) show solid/liquid interface formation when the roller is engaged. (e–h) show solid/liquid interface formation when the roller is raised 500 μm above the part including fluid buildup and air entrapment predicted via simulation. (i–l) show the ability to print multi-material layers supported by fluid and held at the liquid surface via anchoring points at the periphery of the liquid layer. The CU Buffalo logo is supported by a cross of VeroMagenta (the pink region visible in i–l) surrounded by liquid. A head voltage of 19 V was used with the non-solidifying liquid channel. (For interpretation of the references to color in this figure legend, the reader is referred to the web version of this article.)

to fully encapsulate (“cap”) a liquid region with solid material. Printed micro/milli-fluidic channels were found to be most accurate to their design dimensions when printed parallel to the printhead direction of motion which reduces the liquid fingers effect. Minimum repeatable channel design print size was 250 × 108 μm (W × H) for channels printed 45°, and perpendicular to the printhead direction of motion and was 250 × 81 μm for channels printed parallel to the printhead direction of motion. Printed channel cross-sectional areas were less than 60% that of the design channel cross-sectional areas due to the described liquid finger phenomenon. Design rules and fundamentals of liquid–solid co-printing are repeated below for clarity:

1. Select the head voltage to *underjet* liquid in order to better contain liquid by the solid matrix; 19 V is a recommended setting for Stratasys PolyJet systems but users should characterize their system similar to Fig. 6 to verify
2. When *overjetting*, the roller drags liquid into the solid matrix resulting in *liquid fingers* that are on the size order of 300 μm for a circular channel of radius 500 μm. Channels printed parallel to the printhead direction of motion can reduce the effect of liquid fingers
3. Full capping layer encapsulation of a liquid surface occurs at $N \geq 5$ print layers (135 μm)

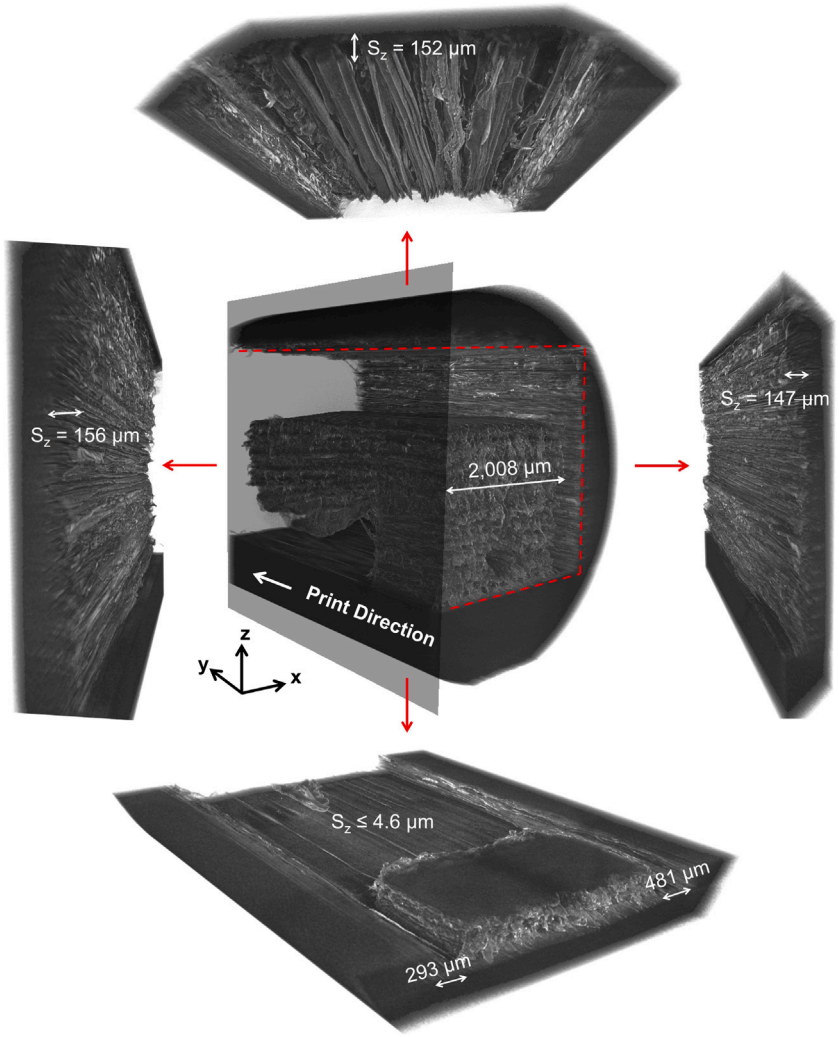

Fig. 12. Milli-Fluidic Channel Wall Characteristics — x-ray micro-computed tomography images of a 3D multi-material liquid-printed internal hanging beam structure (TangoBlack+) fabricated inside a 3 mm × 3 mm milli-channel (VeroClear). Channels were evacuated of liquid to achieve sufficient imaging contrast between void space and solid polymer. Single sided arrows show zoomed in side walls for surface characterization. Double sided arrows on the top, right, and left sidewalls show the maximum surface peak height, S_z, extracted from XRM data as a measure of the surface roughness. The double sided arrows on the bottom side wall denote the spacing between central beam and the wall. A head voltage of 24 V was used to ensure milli-channel dimensionality.

4. If the cured photo-resin droplet density is *less dense* than that of the non photo-curable liquid, then the cured droplet can be freely supported by the liquid as the buoyancy force alone can support the cured droplet
5. If the cured photo-resin droplet density is *more dense* than that of the non photo-curable liquid, then the cured droplet *may* be supported by the non photo-curable liquid's surface tension. However, surface deformations due to roller and droplet impacts create a variable surface tension force that can cause a droplet to sink. The best practice is to use attachment points to the solid matrix when possible in this situation
6. The minimum repeatable channel cross-section (W × H) is 250 × 108 µm without regard for part placement orientation
7. The minimum repeatable channel cross-section is 250 × 81 µm when the channel is oriented parallel to the printhead direction of motion
8. Printed microfluidic channel cross-sectional areas are less than 60% that of the design channel cross-sectional areas due to the liquid finger phenomenon.

Liquid–solid co-printing requires virtually no post-processing to remove liquid from channels (with the exception of input and output ports to purge channels) and eliminates the need for heat treatments common in the use of MJM for micro/mesofluidic channels. Complex 3D multi-material micro/mesofluidic systems, such as the integrated one-way flap valve in this study, demonstrate the versatility of this print process. More generally, this work provides the framework to utilize liquids as material jetting working materials. Here, liquid can be either a sacrificial material, as in micro/mesofluidic channels, or it can be permanently embedded in a part at print time, as in hydraulic robots or reagent placement in a microchannel. To our knowledge, this is the first work to explain the mechanisms that underpin using liquid as a support material, as well as extensively characterize the liquid–solid co-printing print process. We envision liquid–solid co-printing as a toolbox to enable simple and rapid fabrication of intricate 3D, multi-material micro/mesofluidic systems.

6. Materials and methods

6.1. Design and fabrication of micro/mesofluidics

Micro/mesofluidic CAD designs were constructed using Autodesk Fusion 360. Figure S1 illustrates the design processes. Solid and liquid bodies were created allowing for individual material allocation. A Stratasys J750 was used to print the CAD designs with material

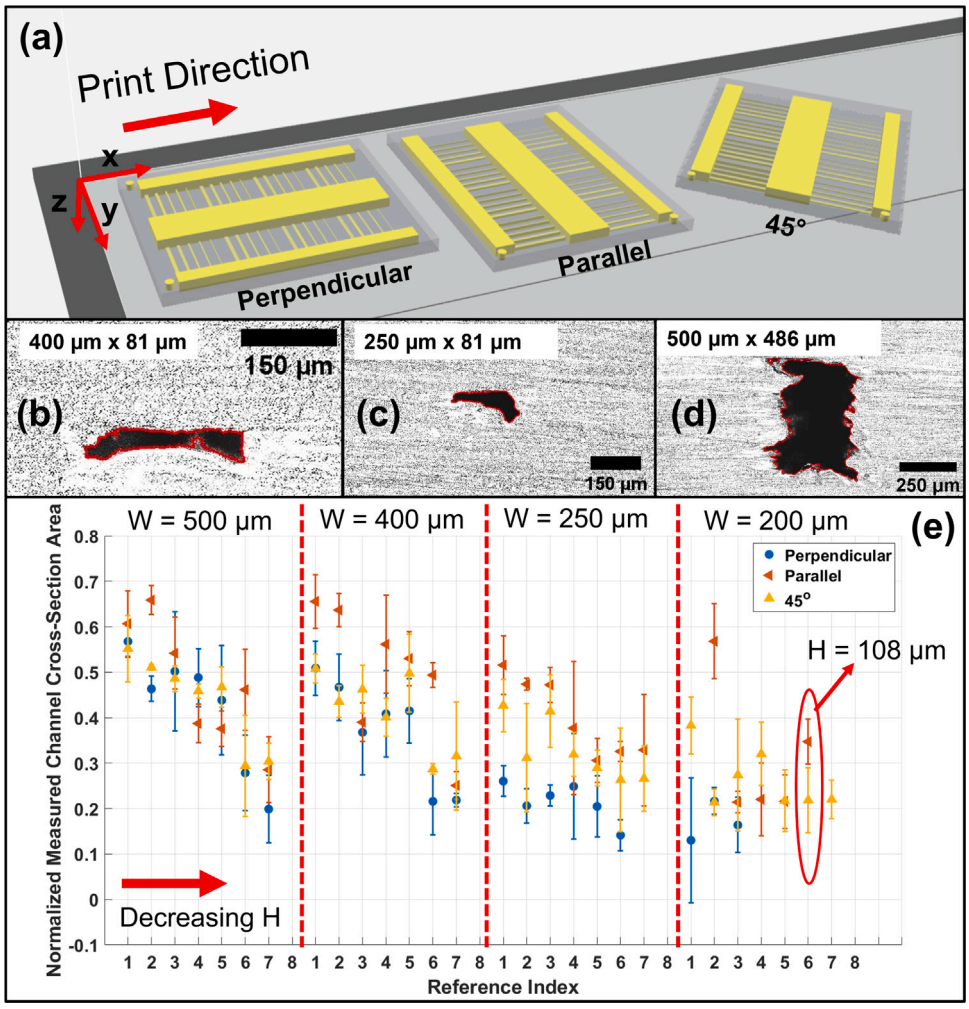

Fig. 13. Print Resolution Analysis — illustrates the effect of part placement orientation on the resulting channel cross-sections for various channel cross-section designs. (a) depicts the CAD design file used to test print-orientation dependency; channels are placed perpendicular, parallel, and 45° to the printhead direction of motion. (b–d) show optical profilometry images of select channel dimensions with the computed channel cross-section boundary highlighted in red. (e) shows the effect of channel orientation with respect to the printhead direction of motion on the resulting channel cross-sectional area normalized to the design cross-sectional area. Error bars represent the standard deviation from n = 3 samples for each channel orientation. Channels were cross-sectioned in accordance with the method described in Section 6.2. Channels that were closed (no flow path) are assigned a normalized cross-section area of 0. The reference index is defined by a monotonically increasing vector in which each block of 8 corresponds to the same design channel width and increasing the reference index within a block implies a decreasing design channel height. Table S1 provides a means to de-reference the index where reference index = 1 corresponds to (row,column) = (1,N), reference index = 8 corresponds to (row,column) = (8,N) where each *N* block of reference indices corresponds to the same design channel width. For example, the first block corresponds to a channel design of W = 500 μm where reference indices 1–8 are H = 486, 351, 270, 216, 162, 108, 81, and 27 μm respectively. A head voltage of 19 V was used.

allocation for each STL set in the Grabcad Print software. We note the ease in design and material allocation of the liquid–solid co-printing print process. Once printed, 19 gauge syringe needles were fitted to the channel ports and the channels were purged of liquid by flushing with distilled water. For optimal VeroClear transparency, parts were then post-processed with wet sanding and application of a crystal clear enamel (Rust-Oleum) to enhance the optical transparency of the VeroClear resin. Print time for a 50.8 mm × 101.3 mm × 3 mm part was less than 30 min.

6.2. Channel cross-section analysis

Channel cross-sectioning was performed by creating a hairline cut across the sample using a Trotec CO_2 laser cutter with a 1.5 inch CO_2 lens. Hairline cuts were performed at 3 equally spaced regions along the 8 mm long channel to better sample the channel cross-section. The laser cuts through the VeroClear polymer, but can locally melt surrounding regions of the cut. As such, wet sanding with 1000 grit sand paper was used to mechanically remove the melted laser ablation region allowing imaging of the channel cross-section not affected by the hairline cut. Channels were then pressure washed with water to remove internal debris. After pressure washing, pressurized air was passed through each channel to purge liquid from the channels. A Keyence VK-X1100 optical profilometer was then used to image each channel cross-section. Channel cross-sections were measured using custom MATLAB scripts to trace the boundaries of the channels and compute their cross-sectional areas.

6.3. Printer configuration for liquid–solid co-printing

A Stratasys J750 printhead consists of fluid reservoirs, microfluidic channels, piezoelectric thin film actuators, and open nozzles. Upon an applied voltage pulse, the piezoelectric thin film oscillates which generates acoustic waves in the fluid. These waves reflect off of the chamber and generate a pressure wave that ejects micro-droplets of fluid (10 to 100 μm in diameter) from the nozzle [79]. The Stratasys J750 system has a print resolution of 600 dpi, 300 dpi, and 27 μm for

x,y, and z directions respectively where dpi is dots per inch. Additionally, the Stratasys J750 is a multi-material system capable of printing simultaneously with 7 different materials.

Liquid–solid co-printing demonstrated in this work uses Stratasys "model cleaning fluid", which is composed primarily of polyethylene glycol according to the material safety datasheet, as a printable, non photo-curable liquid. Here, we summarize the printer configuration protocol of MacCurdy et al. for liquid printing [36]. The Stratasys J750 printer will not accept cleaning fluid as an appropriate working material; as such, the system can be spoofed by replacing the RFID chip in the cleaning fluid cartridge with one from a different model material. We used an RFID chip from a full, unused Tango+ model material cartridge. Material jetting printers deposit droplets of ink by modulating a piezoelectric element with a complex voltage waveform [79]. The Stratasys J750 does not allow access to the internal piezoelectric driving waveform, but it does allow the user to adjust the waveform magnitude via manual entries in the printhead voltage calibration procedure. Thus, the user can optimize the amount of jetted liquid to fit their application.

The Stratasys J750 can print in both STL and voxel modes. STL mode accepts standard STL inputs as discussed previously. In voxel model, a .png stack is used to define the material of each three-dimensional solid unit cell or "voxel" in a design file. Custom MATLAB scripts were used to generate voxel designs. Additionally, a rotating drum, known as the "roller", smooths jetted droplets and removes excess jetted material upon each print pass. Under normal print operation, the roller is always engaged and in contact with each print pass. To index the roller up to prevent the roller from being in contact with each print pass, the *starting height* is changed in the *motor control* drop down menu of the Stratasys J750 printer software when in maintenance mode. It is important to take note of the original starting height in order to revert back to normal print operation with the roller engaged.

6.4. High speed imaging of meso-scale droplet impacts

High speed imaging of meso-scale droplet impact was performed using a Phantom V710 high speed camera. As shown in figure S2, a Chemyx Fusion 101 syringe pump is used to drop photocuring or non photocuring resins above a petri dish of non-solidifying liquid. The Phantom V710 high speed camera is mounted at a 24° angle from the plane of the non-solidifying liquid surface. A Cree XLamp CXB3590 high power LED is used for illumination. World coordinates are obtained by applying the following transformations [64] to correct for the angle of the image plane:

$$\frac{l_x sin(\theta)}{n_x} = \frac{l_o}{n_o} \tag{14}$$

$$\frac{l_y}{n_y} = \frac{l_o}{n_o} \tag{15}$$

$$\frac{l_z cos(\theta)}{n_z} = \frac{l_o}{n_o} \tag{16}$$

where l_o is the real calibration object size corresponding to n_o pixels in the image, l_x is the unknown object size in the $\times$-direction corresponding to n_x pixels in the image, l_z is the unknown object size in the z-direction corresponding to n_z pixels in the image, and θ is the tilt of the high speed camera.

6.5. Photo-resin rheology

Accurate modeling of droplet–liquid interactions requires fluid properties of Stratasys resins which are not readily available through datasheets. Liquid density was measured by sampling 100 μL using a P100 micro-pipette and weighing it on a Ohaus Adventurer microbalance with three sample replicates. Surface tension was measured using the pendant drop method [80] according to Bagalkot et al. with three sample replicates. Cured resin densities were provided by Stratasys datasheets. Viscosity was measured using a TA Instruments AR-G2 rheometer by varying shear from 0 to 500 1/s at 25, 45, and 75 °C. Table S2 shows the resultant average fluid properties at 25 °C for different Stratasys resins.

6.6. Fluidic characterization

Fluidic characterization of micro/mesofluidic devices was performed using a custom setup. Flow was sourced using a Chemyx Fusion 101 syringe pump and the corresponding pressure was measured using 3 and/or 30 psi max Prosense pressure transducers. Fluidic resistance of the tubing was minimized by using a T-connector to place the pressure transducer as close as possible to the channel inlet port. Pressure data was collected at 100 Hz using a LabJack data acquisition unit and the data was analyzed with custom MATLAB scripts.

Data and material availability

All data needed to evaluate the conclusions in the paper are present in the paper and/or the Supplementary Materials as well as provided in the Matter Assembly Lab's public github repository (https://github.com/MacCurdyLab). Additional data related to this paper may be requested from the corresponding author.

CRediT authorship contribution statement

Brandon Hayes: Writing – review & editing, Writing – original draft, Validation, Methodology, Investigation, Formal analysis, Data curation, Conceptualization. **Travis Hainsworth:** Methodology, Formal analysis, Data curation. **Robert MacCurdy:** Writing – review & editing, Supervision, Project administration, Funding acquisition, Conceptualization.

Declaration of competing interest

No author associated with this paper has disclosed any potential or pertinent conflicts which may be perceived to have impending conflict with this work. For full disclosure statements refer to https://doi.org/10.1016/j.addma.2022.102785.

Acknowledgments

The authors would like to thank Joe Dragavon and the BioFrontiers Institute for laser confocal support; Kristine Fischenich and Adrian Gestos for micro-CT analysis performed at MIMIC, CU Boulder (RRID:SCR_019307); Festo USA for providing fluid metrology equipment used in this study; and Lawrence Smith for help with fluid metrology setup and printed capillary images. This work utilized the Summit supercomputer, which is supported by the National Science Foundation, USA (awards ACI-1532235 and ACI-1532236), the University of Colorado Boulder, USA, and Colorado State University, USA. The Summit supercomputer is a joint effort of the University of Colorado Boulder and Colorado State University.

Funding

This work is supported by startup funds to R. MacCurdy provided by the University of Colorado Boulder, USA as well as the National Science Foundation, USA Graduate Research Fellowship under Grant No. DGE 1650115. Any opinion, findings, and conclusions or recommendations expressed in this material are those of the author(s) and do not necessarily reflect the views of the National Science Foundation.

Appendix A. Supplementary data

The supplementary material includes a table of PolyJet material properties, additional simulation results, and additional channel experiments.

Supplementary material related to this article can be found online at https://doi.org/10.1016/j.addma.2022.102785.

References

[1] T. Wohlers, T. Gornet, History of additive manufacturing, in: Wohlers Report, Vol. 24, No. 2014, 2014, p. 118.

[2] G.D. O'Neil, Toward single-step production of functional electrochemical devices using 3D printing: Progress, challenges, and opportunities, Curr. Opin. Electrochem. 20 (2020) 60–65.

[3] A.H. Espera, J.R.C. Dizon, Q. Chen, R.C. Advincula, 3D -Printing and advanced manufacturing for electronics, Progr. Addit. Manuf. (2019) 1–23.

[4] J.Z. Gul, M. Sajid, M.M. Rehman, G.U. Siddiqui, I. Shah, K.-H. Kim, J.-W. Lee, K.H. Choi, 3D Printing for soft robotics–a review, Sci. Technol. Adv. Mater. 19 (1) (2018) 243–262.

[5] V. Romanov, R. Samuel, M. Chaharlang, A.R. Jafek, A. Frost, B.K. Gale, FDM 3D printing of high-pressure, heat-resistant, transparent microfluidic devices, Anal. Chem. 90 (17) (2018) 10450–10456, http://dx.doi.org/10.1021/acs.analchem.8b02356.

[6] P.J. Kitson, M.H. Rosnes, V. Sans, V. Dragone, L. Cronin, Configurable 3D -printed millifluidic and microfluidic 'lab on a chip' reactionware devices, Lab A Chip 12 (18) (2012) 3267–3271.

[7] H. Gong, A.T. Woolley, G.P. Nordin, High density 3D printed microfluidic valves, pumps, and multiplexers, Lab Chip 16 (2016) 2450–2458, http://dx.doi.org/10.1039/C6LC00565A.

[8] Q. Zhang, X. Peng, S. Weng, R. Zhang, D. Fang, R. Zhao, H.J. Qi, Self-adaptive flexible valve as passive flow regulator, Extrem. Mech. Lett. 39 (2020) 100824.

[9] H. Gong, B.P. Bickham, A.T. Woolley, G.P. Nordin, Custom 3D printer and resin for 18 um × 20 um microfluidic flow channels, Lab Chip 17 (2017) 2899–2909, http://dx.doi.org/10.1039/C7LC00644F.

[10] S. Razavi Bazaz, O. Rouhi, M.A. Raoufi, F. Ejeian, M. Asadnia, D. Jin, M. Ebrahimi Warkiani, 3D Printing of inertial microfluidic devices, Sci. Rep. 10 (1) (2020) 5929, http://dx.doi.org/10.1038/s41598-020-62569-9.

[11] B.N. Peele, T.J. Wallin, H. Zhao, R.F. Shepherd, 3D Printing antagonistic systems of artificial muscle using projection stereolithography, Bioinspiration Biomim. 10 (5) (2015) 055003.

[12] G. van der Velden, D. Fan, U. Staufer, Fabrication of a microfluidic device by using two-photon lithography on a positive photoresist, Micro Nano Eng. 7 (2020) 100054, http://dx.doi.org/10.1016/j.mne.2020.100054, URL https://www.sciencedirect.com/science/article/pii/S2590007220300095.

[13] H. Horng, K. O'Brien, A. Lamont, R.D. Sochol, T.J. Pfefer, Y. Chen, 3D Printed vascular phantoms for high-resolution biophotonic image quality assessment via direct laser writing, Opt. Lett. 46 (8) (2021) 1987–1990, http://dx.doi.org/10.1364/OL.412849, URL http://ol.osa.org/abstract.cfm?URI=ol-46-8-1987.

[14] A.T. Alsharhan, O.M. Young, X. Xu, A.J. Stair, R.D. Sochol, Integrated 3D printed microfluidic circuitry and soft microrobotic actuators via in situ direct laser writing, J. Micromech. Microeng. 31 (4) (2021) 044001.

[15] T. Calais, N.D. Sanandiya, S. Jain, E.V. Kanhere, S. Kumar, R.C.-H. Yeow, P. Valdivia y Alvarado, Freeform liquid 3D printing of soft functional components for soft robotics, ACS Appl. Mater. Interfaces (2021).

[16] D.B. Kolesky, R.L. Truby, A. Gladman, T.A. Busbee, K.A. Homan, J.A. Lewis, 3D Bioprinting of vascularized, heterogeneous cell-laden tissue constructs, Adv. Mater. 26 (19) (2014) 3124–3130.

[17] M.A. Skylar-Scott, J. Mueller, C.W. Visser, J.A. Lewis, Voxelated soft matter via multimaterial multinozzle 3D printing, Nature 575 (7782) (2019) 330–335.

[18] N. Anscombe, Direct laser writing, Nat. Photonics 4 (1) (2010) 22–23.

[19] D.A. Walker, J.L. Hedrick, C.A. Mirkin, Rapid, large-volume, thermally controlled 3D printing using a mobile liquid interface, Science 366 (6463) (2019) 360–364, http://dx.doi.org/10.1126/science.aax1562, arXiv:https://www.science.org/doi/pdf/10.1126/science.aax1562, URL https://www.science.org/doi/abs/10.1126/science.aax1562.

[20] G.I. Peterson, J.J. Schwartz, D. Zhang, B.M. Weiss, M.A. Ganter, D.W. Storti, A.J. Boydston, Production of materials with spatially-controlled cross-link density via vat photopolymerization, ACS Appl. Mater. Interfaces 8 (42) (2016) 29037–29043.

[21] A. Muralidharan, A.C. Uzcategui, R.R. McLeod, S.J. Bryant, Stereolithographic 3D printing for deterministic control over integration in dual-material composites, Adv. Mater. Technol. 4 (11) (2019) 1900592.

[22] Q. Ge, Z. Chen, J. Cheng, B. Zhang, Y.-F. Zhang, H. Li, X. He, C. Yuan, J. Liu, S. Magdassi, et al., 3D Printing of highly stretchable hydrogel with diverse UV curable polymers, Sci. Adv. 7 (2) (2021) eaba4261.

[23] F. Mayer, S. Richter, J. Westhauser, E. Blasco, C. Barner-Kowollik, M. Wegener, Multimaterial 3D laser microprinting using an integrated microfluidic system, Sci. Adv. 5 (2) (2019) eaau9160, http://dx.doi.org/10.1126/sciadv.aau9160, arXiv:https://www.science.org/doi/pdf/10.1126/sciadv.aau9160, URL https://www.science.org/doi/abs/10.1126/sciadv.aau9160.

[24] A.C. Lamont, M.A. Restaino, M.J. Kim, R.D. Sochol, A facile multi-material direct laser writing strategy, Lab Chip 19 (2019) 2340–2345, http://dx.doi.org/10.1039/C9LC00398C.

[25] C. Tawk, G. Alici, A review of 3D -printable soft pneumatic actuators and sensors: Research challenges and opportunities, Adv. Intell. Syst. (2021) 2000223.

[26] W. Gao, S. Emaminejad, H.Y.Y. Nyein, S. Challa, K. Chen, A. Peck, H.M. Fahad, H. Ota, H. Shiraki, D. Kiriya, et al., Fully integrated wearable sensor arrays for multiplexed in situ perspiration analysis, Nature 529 (7587) (2016) 509–514.

[27] T.R. Ray, J. Choi, A.J. Bandodkar, S. Krishnan, P. Gutruf, L. Tian, R. Ghaffari, J.A. Rogers, Bio-integrated wearable systems: a comprehensive review, Chem. Rev. 119 (8) (2019) 5461–5533.

[28] D.J. Preston, P. Rothemund, H.J. Jiang, M.P. Nemitz, J. Rawson, Z. Suo, G.M. Whitesides, Digital logic for soft devices, Proc. Natl. Acad. Sci. 116 (16) (2019) 7750–7759, http://dx.doi.org/10.1073/pnas.1820672116, arXiv:https://www.pnas.org/content/116/16/7750.full.pdf, URL https://www.pnas.org/content/116/16/7750.

[29] P. Rothemund, A. Ainla, L. Belding, D.J. Preston, S. Kurihara, Z. Suo, G.M. Whitesides, A soft, bistable valve for autonomous control of soft actuators, Science Robotics 3 (16) (2018) eaar7986, http://dx.doi.org/10.1126/scirobotics.aar7986, arXiv:https://www.science.org/doi/pdf/10.1126/scirobotics.aar7986, URL https://www.science.org/doi/abs/10.1126/scirobotics.aar7986.

[30] T. Ranzani, S. Russo, N.W. Bartlett, M. Wehner, R.J. Wood, Increasing the dimensionality of soft microstructures through injection-induced self-folding, Adv. Mater. 30 (38) (2018) 1802739, http://dx.doi.org/10.1002/adma.201802739, arXiv:https://onlinelibrary.wiley.com/doi/pdf/10.1002/adma.201802739, URL https://onlinelibrary.wiley.com/doi/abs/10.1002/adma.201802739.

[31] D. Dikovsky, S. Shtilerman, System and method for fabricating a body part model using multi-material additive manufacturing, 2018, Google Patents, US Patent 9,999, 509.

[32] R.N. Leyden, J.S. Thayer, B.J.L. Bedal, T.A. Almquist, C.W. Hull, J.M. Earl, T.A. Kerekes, D.R. Smalley, C.M. Merot, R.P. Fedchenko, M.S. Lockard, T.H. Pang, D.T. That, Selective deposition modeling method and apparatus for forming three-dimensional objects and supports, 2001, Google Patents, US Patent 6, 193, 923.

[33] A.D. Castiaux, E.A. Hayter, M.E. Bunn, S.R. Martin, D.M. Spence, PolyJet 3D -printed enclosed microfluidic channels without photocurable supports, Anal. Chem. 91 (10) (2019) 6910–6917.

[34] J.D. Hubbard, R. Acevedo, K.M. Edwards, A.T. Alsharhan, Z. Wen, J. Landry, K. Wang, S. Schaffer, R.D. Sochol, Fully 3D -printed soft robots with integrated fluidic circuitry, Sci. Adv. 7 (29) (2021) http://dx.doi.org/10.1126/sciadv.abe5257, arXiv:https://advances.sciencemag.org/content/7/29/eabe5257.full.pdf, URL https://advances.sciencemag.org/content/7/29/eabe5257.

[35] R.D. Sochol, E. Sweet, C.C. Glick, S. Venkatesh, A. Avetisyan, K.F. Ekman, A. Raulinaitis, A. Tsai, A. Wienkers, K. Korner, K. Hanson, A. Long, B.J. Hightower, G. Slatton, D.C. Burnett, T.L. Massey, K. Iwai, L.P. Lee, K.S.J. Pister, L. Lin, 3D Printed microfluidic circuitry via multijet-based additive manufacturing, Lab Chip 16 (2016) 668–678, http://dx.doi.org/10.1039/C5LC01389E.

[36] R. MacCurdy, R. Katzschmann, Y. Kim, D. Rus, Printable hydraulics: A method for fabricating robots by 3D co-printing solids and liquids, in: IEEE International Conference on Robotics and Automation, Vol. 2, ICRA, 2016.

[37] A. Alfadhel, J. Ouyang, C.G. Mahajan, F. Forouzandeh, D. Cormier, D.A. Borkholder, Inkjet printed polyethylene glycol as a fugitive ink for the fabrication of flexible microfluidic systems, Mater. Des. 150 (2018) 182–187, http://dx.doi.org/10.1016/j.matdes.2018.04.013, URL http://www.sciencedirect.com/science/article/pii/S0264127518302843.

[38] E.H. Childs, A.V. Latchman, A.C. Lamont, J.D. Hubbard, R.D. Sochol, Additive assembly for PolyJet-based multi-material 3D printed microfluidics, J. Microelectromech. Syst. 29 (5) (2020) 1094–1096, http://dx.doi.org/10.1109/JMEMS.2020.3003858.

[39] S.J. Keating, M.I. Gariboldi, W.G. Patrick, S. Sharma, D.S. Kong, N. Oxman, 3D Printed multimaterial microfluidic valve, PLoS One 11 (8) (2016) 1–12, http://dx.doi.org/10.1371/journal.pone.0160624.

[40] Y. Guo, H.S. Patanwala, B. Bognet, A.W. Ma, Inkjet and inkjet-based 3D printing: connecting fluid properties and printing performance, Rapid Prototyp. J. (2017).

[41] A. Hosny, S.J. Keating, J.D. Dilley, B. Ripley, T. Kelil, S. Pieper, D. Kolb, C. Bader, A.-M. Pobloth, M. Griffin, R. Nezafat, G. Duda, E.A. Chiocca, J.R. Stone, J.S. Michaelson, M.N. Dean, N. Oxman, J.C. Weaver, From improved diagnostics to presurgical planning: High-resolution functionally graded multimaterial 3D printing of biomedical tomographic data sets, in: 3D Printing and Additive Manufacturing, Vol. 5, No. 2, 2018, pp. 103–113, http://dx.doi.org/10.1089/3dp.2017.0140.

[42] R. Worsley, L. Pimpolari, D. McManus, N. Ge, R. Ionescu, J.A. Wittkopf, A. Alieva, G. Basso, M. Macucci, G. Iannaccone, et al., All-2D material inkjet-printed capacitors: toward fully printed integrated circuits, Acs Nano 13 (1) (2018) 54–60.

[43] T. Carey, S. Cacovich, G. Divitini, J. Ren, A. Mansouri, J.M. Kim, C. Wang, C. Ducati, R. Sordan, F. Torrisi, Fully inkjet-printed two-dimensional material field-effect heterojunctions for wearable and textile electronics, Nature Commun. 8 (1) (2017) 1202.

[44] T. Pinto, C. Chen, C. Pinger, X. Tan, 3D -Printed liquid metal-based stretchable conductors and pressure sensors, Smart Mater. Struct. 30 (9) (2021) 095005.

[45] Y. Wei, Y. Chen, Y. Yang, Y. Li, Novel design and 3-D printing of nonassembly controllable pneumatic robots, IEEE/ASME Trans. Mechatronics 21 (2) (2016) 649–659, http://dx.doi.org/10.1109/TMECH.2015.2492623.

[46] S. Coros, B. Thomaszewski, G. Noris, S. Sueda, M. Forberg, R.W. Sumner, W. Matusik, B. Bickel, Computational design of mechanical characters, ACM Trans. Graph. 32 (4) (2013) 83.

[47] A. Alfadhel, J. Ouyang, C.G. Mahajan, F. Forouzandeh, D. Cormier, D.A. Borkholder, Inkjet printed polyethylene glycol as a fugitive ink for the fabrication of flexible microfluidic systems, Mater. Des. 150 (2018) 182–187, http://dx.doi.org/10.1016/j.matdes.2018.04.013, URL https://www.sciencedirect.com/science/article/pii/S0264127518302843.

[48] D. Therriault, R. Shepherd, S. White, J. Lewis, Fugitive inks for direct-write assembly of three-dimensional microvascular networks, Adv. Mater. 17 (4) (2005) 395–399, http://dx.doi.org/10.1002/adma.200400481, arXiv:https://onlinelibrary.wiley.com/doi/pdf/10.1002/adma.200400481, URL https://onlinelibrary.wiley.com/doi/abs/10.1002/adma.200400481.

[49] D.B. Kolesky, R.L. Truby, A.S. Gladman, T.A. Busbee, K.A. Homan, J.A. Lewis, 3D Bioprinting of vascularized, heterogeneous cell-laden tissue constructs, Adv. Mater. 26 (19) (2014) 3124–3130, http://dx.doi.org/10.1002/adma.201305506, arXiv:https://onlinelibrary.wiley.com/doi/pdf/10.1002/adma.201305506, URL https://onlinelibrary.wiley.com/doi/abs/10.1002/adma.201305506.

[50] D.B. Kolesky, K.A. Homan, M.A. Skylar-Scott, J.A. Lewis, Three-dimensional bioprinting of thick vascularized tissues, Proc. Natl. Acad. Sci. 113 (12) (2016) 3179–3184, http://dx.doi.org/10.1073/pnas.1521342113, arXiv:https://www.pnas.org/content/113/12/3179.full.pdf, URL https://www.pnas.org/content/113/12/3179.

[51] A. Mamidanna, C. Lefky, O. Hildreth, Drop-on-demand printed microfluidics device with sensing electrodes using silver and PDMS reactive inks, Microfluid. Nanofluid. 21 (11) (2017) 172, http://dx.doi.org/10.1007/s10404-017-2010-8.

[52] D.P. Parekh, C. Ladd, L. Panich, K. Moussa, M.D. Dickey, 3D Printing of liquid metals as fugitive inks for fabrication of 3D microfluidic channels, Lab Chip 16 (2016) 1812–1820, http://dx.doi.org/10.1039/C6LC00198J.

[53] M.K. Gelber, R. Bhargava, Monolithic multilayer microfluidics via sacrificial molding of 3D -printed isomalt, Lab Chip 15 (2015) 1736–1741, http://dx.doi.org/10.1039/C4LC01392A.

[54] S. Waheed, J.M. Cabot, N.P. Macdonald, T. Lewis, R.M. Guijt, B. Paull, M.C. Breadmore, 3D Printed microfluidic devices: enablers and barriers, Lab Chip 16 (2016) 1993–2013, http://dx.doi.org/10.1039/C6LC00284F.

[55] A.D. Castiaux, M.A. Selemani, M.A. Ward, R.S. Martin, Fully 3D printed fluidic devices with integrated valves and pumps for flow injection analysis, Anal. Methods (2021) http://dx.doi.org/10.1039/D1AY01569A.

[56] C. Chen, B.T. Mehl, A.S. Munshi, A.D. Townsend, D.M. Spence, R.S. Martin, 3D -Printed microfluidic devices: fabrication, advantages and limitations—a mini review, Anal. Methods 8 (2016) 6005–6012, http://dx.doi.org/10.1039/C6AY01671E.

[57] F. Li, P. Smejkal, N.P. Macdonald, R.M. Guijt, M.C. Breadmore, One-step fabrication of a microfluidic device with an integrated membrane and embedded reagents by multimaterial 3D printing, Anal. Chem. 89 (8) (2017) 4701–4707, http://dx.doi.org/10.1021/acs.analchem.7b00409, PMID: 28322552.

[58] C. Hirt, B. Nichols, Volume of fluid (VOF) method for the dynamics of free boundaries, J. Comput. Phys. 39 (1) (1981) 201–225, http://dx.doi.org/10.1016/0021-9991(81)90145-5, URL https://www.sciencedirect.com/science/article/pii/0021999181901455.

[59] J. Brackbill, D. Kothe, C. Zemach, A continuum method for modeling surface tension, J. Comput. Phys. 100 (2) (1992) 335–354, http://dx.doi.org/10.1016/0021-9991(92)90240-Y, URL https://www.sciencedirect.com/science/article/pii/002199919290240Y.

[60] H.G. Weller, A New Approach to VOF-Based Interface Capturing Methods for Incompressible and Compressible Flow, Vol. 4, Report TR/HGW, OpenCFD Ltd. 2008, p. 35.

[61] L. Wang, K. Wang, H. Hu, Y. Luo, L. Chen, S. Chen, B. Lu, Inkjet jet failures detection and droplets speed monitoring using piezo self-sensing, Sensors Actuators A 313 (2020) 112178, http://dx.doi.org/10.1016/j.sna.2020.112178, URL https://www.sciencedirect.com/science/article/pii/S0924424719323490.

[62] L. Zorzetto, L. Andena, F. Briatico-Vangosa, L. De Noni, J.-M. Thomassin, C. Jérôme, Q. Grossman, A. Mertens, R. Weinkamer, M. Rink, D. Ruffoni, Properties and role of interfaces in multimaterial 3D printed composites, Sci. Rep. 10 (1) (2020) 22285, http://dx.doi.org/10.1038/s41598-020-79230-0.

[63] J. Mueller, D. Courty, M. Spielhofer, R. Spolenak, K. Shea, Mechanical properties of interfaces in inkjet 3D printed single- and multi-material parts, in: 3D Printing and Additive Manufacturing, Vol. 4, No. 4, 2017, pp. 193–199, http://dx.doi.org/10.1089/3dp.2017.0038.

[64] Z. Che, O.K. Matar, Impact of droplets on immiscible liquid films, Soft Matter 14 (2018) 1540–1551, http://dx.doi.org/10.1039/C7SM02089A.

[65] L.V. Zhang, J. Toole, K. Fezzaa, R.D. Deegan, Evolution of the ejecta sheet from the impact of a drop with a deep pool, J. Fluid Mech. 690 (2012) 5–15, http://dx.doi.org/10.1017/jfm.2011.396.

[66] H. Yi, L. Qi, J. Luo, D. Zhang, H. Li, X. Hou, Effect of the surface morphology of solidified droplet on remelting between neighboring aluminum droplets, Int. J. Mach. Tools Manuf. 130–131 (2018) 1–11, http://dx.doi.org/10.1016/j.ijmachtools.2018.03.006, URL https://www.sciencedirect.com/science/article/pii/S089069551830066X.

[67] M. Liu, H. Yi, H. Cao, R. Huang, L. Jia, Heat accumulation effect in metal droplet-based 3D printing: Evolution mechanism and elimination strategy, Addit. Manuf. 48 (2021) 102413, http://dx.doi.org/10.1016/j.addma.2021.102413, URL https://www.sciencedirect.com/science/article/pii/S2214860421005662.

[68] D. Banks, C. Ajawara, R. Sanchez, H. Surti, G. Aguilar, Effects of drop and film viscosity on drop impacts onto thin films, At. Sprays 23 (6) (2013) 525–540.

[69] B. Widom, Capillarity and wetting phenomena: Drops, bubbles, pearls, waves, Phys. Today 57 (12) (2004) 66–67, http://dx.doi.org/10.1063/1.1878340.

[70] J.S. Lee, B.M. Weon, S.J. Park, J.T. Kim, J. Pyo, K. Fezzaa, J.H. Je, Air evolution during drop impact on liquid pool, Sci. Rep. 10 (1) (2020) 5790, http://dx.doi.org/10.1038/s41598-020-62705-5.

[71] G. Pendharkar, R. Deshmukh, R. Patrikar, Investigation of surface roughness effects on fluid flow in passive micromixer, Microsyst. Technol. 20 (12) (2014) 2261–2269, http://dx.doi.org/10.1007/s00542-013-1957-y.

[72] S. Song, S. Joshi, J. Paik, CMOS-inspired complementary fluidic circuits for soft robots, Adv. Sci. n/a (n/a) 2100924, http://dx.doi.org/10.1002/advs.202100924, arXiv:https://onlinelibrary.wiley.com/doi/pdf/10.1002/advs.202100924, URL https://onlinelibrary.wiley.com/doi/abs/10.1002/advs.202100924.

[73] M. Wehner, R.L. Truby, D.J. Fitzgerald, B. Mosadegh, G.M. Whitesides, J.A. Lewis, R.J. Wood, An integrated design and fabrication strategy for entirely soft, autonomous robots, Nature 536 (7617) (2016) 451–455, http://dx.doi.org/10.1038/nature19100.

[74] M. Prakash, N. Gershenfeld, Microfluidic bubble logic, Science 315 (5813) (2007) 832–835, http://dx.doi.org/10.1126/science.1136907, arXiv:https://www.science.org/doi/pdf/10.1126/science.1136907.

[75] A. Zatopa, S. Walker, Y. Menguc, Fully soft 3D -printed electroactive fluidic valve for soft hydraulic robots, Soft Robotics 5 (3) (2018) 258–271, http://dx.doi.org/10.1089/soro.2017.0019.

[76] D.J. Cocovi-Solberg, M. Rosende, M. Michalec, M. Miró, 3D Printing: The second dawn of lab-on-valve fluidic platforms for automatic (Bio)chemical assays, Anal. Chem. 91 (1) (2019) 1140–1149, http://dx.doi.org/10.1021/acs.analchem.8b04900.

[77] J.M. Zhang, Q. Ji, H. Duan, Three-dimensional printed devices in droplet microfluidics, Micromachines 10 (11) (2019) http://dx.doi.org/10.3390/mi10110754, URL https://www.mdpi.com/2072-666X/10/11/754.

[78] Y. Wang, Y. Zhang, Z. Qiao, W. Wang, A 3D printed Jet mixer for centrifugal microfluidic platforms, Micromachines 11 (7) (2020) http://dx.doi.org/10.3390/mi11070695, URL https://www.mdpi.com/2072-666X/11/7/695.

[79] D.B. Bogy, F.E. Talke, Experimental and theoretical study of wave propagation phenomena in drop-on-demand ink jet devices, IBM J. Res. Dev. 28 (3) (1984) 314–321, http://dx.doi.org/10.1147/rd.283.0314.

[80] N. Bagalkot, A.A. Hamouda, O.M. Isdahl, Dynamic interfacial tension measurement method using axisymmetric drop shape analysis, MethodsX 5 (2018) 676–683, http://dx.doi.org/10.1016/j.mex.2018.06.012, URL https://www.sciencedirect.com/science/article/pii/S2215016118301006.